ARBEITSBERICHT NAB 25-03

Extent and Hydraulic Characteristics of the EDZ around Underground Structures of a Repository for HLW and L/ILW in the Siting Region Nördlich Lägern

January 2025

Nagra | National Cooperative for the Disposal of Radioactive Waste
Hardstrasse 73 | 5430 Wettingen | Switzerland
+41 56 437 11 11 | info@nagra.ch | nagra.ch

nagra.

ARBEITSBERICHT NAB 25-03

Extent and Hydraulic Characteristics of the EDZ around Underground Structures of a Repository for HLW and L/ILW in the Siting Region Nördlich Lägern

January 2025

KEYWORDS
Opalinus Clay, SF/HLW, L/ILW, combined repository, Nördlich Lägern, EDZ, effective hydraulic conductivity, effective porosity

Nagra | **National Cooperative for the Disposal of Radioactive Waste**
Hardstrasse 73 | 5430 Wettingen | Switzerland
+41 56 437 11 11 | info@nagra.ch | nagra.ch

Nagra Arbeitsberichte ("Working Reports") present the results of work in progress that have not necessarily been subject to a comprehensive review. They are intended to provide rapid dissemination of current information.

The report NAB 25-03 has been elaborated by A. Alcolea[1] & P. Marschall[2]

[1] HydroGeoModels AG, Seuzach, Switzerland

[2] Nagra

Executive summary

The EDZ around the backfilled underground structures of a geological repository represents a viable release path for radionuclides dissolved in the porewater of the repository nearfield as well as a possible escape route for corrosion and degradation gases. The efficiency of this release path depends on the shape and extent of the EDZ and on its effective hydraulic conductance (cross-sectional area of the EDZ × effective hydraulic conductivity). Thickness and effective hydraulic conductivity of the EDZ are key parameters in performance assessment and safety assessment modelling.

This report provides the estimated hydraulic properties of the EDZ around three safety-relevant repository components, namely the HLW drifts, the L/ILW caverns and the V3 shaft seals. It is based on fracture network simulations for the provisional repository project at the Haberstal site with the technical repository layout described in the engineering dossier. Following a well-established modelling workflow, the discrete EDZ fracture networks are converted into hydraulic continuum models with heterogeneous distributions of porosity and hydraulic conductivity. In a final step, the complex shape of the EDZ is abstracted towards a simplified representation, amenable to be handled with conventional PA/SA modelling tools.

For each of the three repository components, six different EDZ fracture patterns were analysed, representing sensible EDZ realisations for a wide range of possible stress conditions at repository level. Look-up tables were generated, displaying thickness, equivalent hydraulic conductivity and equivalent porosity of the homogenized EDZ for the HLW drifts, the L/ILW caverns and the shaft seals as input for the PA/SA calculations.

Table of Contents

List of Tables

List of Figures

List of Acronyms

CRC	Core reaction curve
EDZ	Excavation damaged zone
FDEM, FEMDEM	Hybrid finite/discrete element method
GRC	Ground response curve
JO	Jura Ost (siting region)
L/ILW	Low- and intermediate-level waste
NAB	Nagra Work Report
NL	Nördlich Lägern (siting region)
NTB	Nagra Technical Report
PA	Performance assessment
SA	Safety assessment
SCC	Support characteristic curve
SF/HLW	Spent fuel / high level waste
SFOE	Swiss Federal Office of Energy
SGT	Sectoral Plan for Deep Geological Repositories
V3	Shaft seal
ZNO	Zürich Nordost (siting region)

1 Introduction

1.1 Background and motivation

The procedure for selecting the sites for the deep geological repositories in Switzerland was specified in the conceptual part of the Sectoral Plan for Deep Geological Repositories (SGT) (BFE 2008) and consisted of three stages. In Stage 3, the three remaining potential siting regions Jura Ost (JO), Nördlich Lägern (NL) and Zürich Nordost (ZNO) were examined in detail and, where necessary, supplementary geological investigations were performed. The broadened site-specific database formed the basis for selecting the NL siting region for a repository with a section for spent fuel and high-level waste (SF/HLW) and a section for low- and intermediate-level waste (L/ILW), respectively, for which the general licence application has been prepared by the end of 2024.

In the context of the Sectoral Plan the authorities requested a balanced evaluation of the impact of repository induced effects on the long-term safety of the repository for SF/HLW and L/ILW. The key effects to be assessed are the accumulation and release of repository gases, the heat emission of the HLW canisters and the excavation damaged zone (EDZ) around the backfilled underground structures (see also Leupin et al. 2016a, 2016b). As a contribution to the assessment of repository induced effects a generic workflow was developed in SGT – Stage 2, aimed at evaluating the impact of the EDZ on repository performance, both for the HLW and L/ILW repository (Nagra 2014). First, shape and extent of the EDZ were estimated by mechanical fracture network simulations using a hybrid finite/discrete element method (FEMDEM). Extensive numerical analyses were carried out, including sensitivity studies for a variety of SF/HLW and L/ILW repository configurations (Geomechanica 2013). In a second step, the impacts of the EDZ on repository safety were addressed with particular focus on the function of the host rock as a hydraulic barrier. The assessments of the hydraulic aspects were detailed in Alcolea et al. (2014).

The safety case for a deep geological repository at the Haberstal site in the Nördlich Lägern siting region required a site-specific evaluation of the safety-relevant impacts of the EDZ, both for both high-level waste (HLW) and low- and the intermediate-level waste (L/ILW) repository sections. For this, complementary EDZ fracture network simulations were performed, taking into account the local stress conditions at the prospected repository site and using the latest databases on the geomechanical properties of the host rock (Geomechanica 2025). The EDZ fracture network simulations were carried out for the HLW drifts, the L/ILW caverns and for the V3 shaft seals. The modelling results formed the input for quantitative estimates of the hydraulic conductivity of the EDZ, which are documented in the present report and are used within model-based assessments of repository performance (Nagra 2024a,b) and in safety assessment (Nagra 2024c).

1.2 Scope and objectives

The EDZ around the backfilled underground structures of a geological repository represents a viable release path for radionuclides as well as a possible escape route for corrosion and degradation gases. The efficiency of this release path depends on the shape and extent of the EDZ and on its effective hydraulic conductivity. This report provides as input for performance and safety assessment the estimated hydraulic properties of the EDZ around three safety-relevant repository components, namely the HLW drifts, the L/ILW caverns and the V3 shaft seals. It is based on fracture network simulations (Geomechanica 2025) for the provisional repository project at the Haberstal site with the technical repository layout described in the engineering dossier (Nagra 2023a). Following the workflow of Alcolea et al. (2014), the discrete EDZ fracture networks are converted into hydraulic continuum models with heterogeneous distributions of porosity and hydraulic conductivity. In a final step, the complex shape of the EDZ is abstracted towards a simplified representation, amenable to be handled with conventional PA/SA modelling tools.

For each of the three repository components, six different EDZ fracture patterns were analysed, representing a balanced set of EDZ realisations for a wide range of strength and stress conditions at repository level. Look-up tables were generated, displaying thickness, equivalent hydraulic conductivity and equivalent porosity of the homogenized EDZ for the HLW drifts, the L/ILW caverns and the shaft seals as input for the PA/SA calculations.

1.3 Report organisation

Chapter 1 presents the background and motivation for the estimation of hydraulic conductance of the EDZ around the backfilled repository structures. Scope and organization of the report are discussed.

Fundamentals and the basic EDZ modelling workflow are summarized in Chapter 2. This chapter includes a brief history of the workflow development during previous stages of the Sectoral plan.

Chapter 3 presents a summary of the fracture network simulations by Geomechanica (2025), aimed at simulating the EDZ fracture network around the HLW drifts, the L/ILW caverns and the V3 shaft of the proposed repository project at the Haberstal site.

The fracture network simulations provide the geometric input for the calculation of hydraulic conductance of the EDZ in Chapter 4. Equivalent thicknesses, porosities and hydraulic conductivities are derived for the three above mentioned cross-sections. The results are presented in terms of look-up tables, which are easy to use in safety assessment.

The report ends up with a brief summary of the achievements and concluding remarks.

2 The EDZ assessment workflow for PA/SA

A generic workflow was developed in SGT - Stage 2, aimed at evaluating the impact of the EDZ on repository performance, both for the HLW and L/ILW repository (Nagra 2014, Leupin et al. 2016a, b). The same workflow has been pursued in the safety case for a deep geological repository at the Haberstal site in the Nördlich Lägern siting region. The conceptual framework and the key elements of the assessment procedure are described in the following sections.

2.1 Conceptual framework for EDZ fracture closure in Opalinus Clay

Drawing on empirical and experimental evidence about the hydraulic significance of the EDZ during tunnel construction, its evolution during operational times and after backfilling of tunnels (Lanyon et al. 2014, Nagra 2014), a conceptual framework for a quantitative EDZ closure model has been formulated with the following features (see Fig. 2-1):

- The creation of the EDZ is a brittle process, i.e. the increase of the void volume of the damaged rock zone around the excavation is solely attributed to fracture opening, whereas the porosity of non-fractured rock domains remains essentially unchanged during the early times.
- Initially, the newly created EDZ fractures are unsaturated and exposed to atmospheric pressure, whereas the non-fractured rock domains remain saturated and exhibit high matrix suction as a consequence of the high gas entry pressure of the Opalinus Clay. The initial transmissivity of the unsaturated EDZ fractures is controlled by the fracture aperture and can be very high. The matrix conductivity remains essentially unchanged, i.e. it is the same as the conductivity of the intact rock.
- With time, the matric suction in the rock matrix ceases due to the uptake of porewater from outer rock zones and the fractures start to resaturate.
- Porewater uptake in the non-fractured rock zones in response to the reduction of effective stress (drained response) is associated with swelling and consequently with an increase of matrix porosity. This porosity increase of the rock matrix occurs at the expense of the fracture aperture, i.e. the fractures start to close and fracture transmissivity decreases drastically, whereas the hydraulic conductivity of the non-fractured matrix zones increases slightly as a consequence of the porosity increase.
- This process of porosity and conductivity increase of the matrix is associated with a decrease of fracture aperture and transmissivity and progresses until an effective stress equilibrium is reached. This is essentially the case when the pore pressure reaches the static formation pressure.

Extensive experimental evidence was collected in the recent years which confirms the efficiency of EDZ self-sealing processes at the laboratory and in-situ scale (Marschall et al. 2017, Seiphoori 2019, Levasseur et al. 2021, 2023). In the following sections, a heuristic EDZ model is developed that mimics the evolution described above in a simplified manner. The evolution of the hydraulic properties of the EDZ is simulated over the entire period ranging from the early post-excavation phase until static formation pressure recovery.

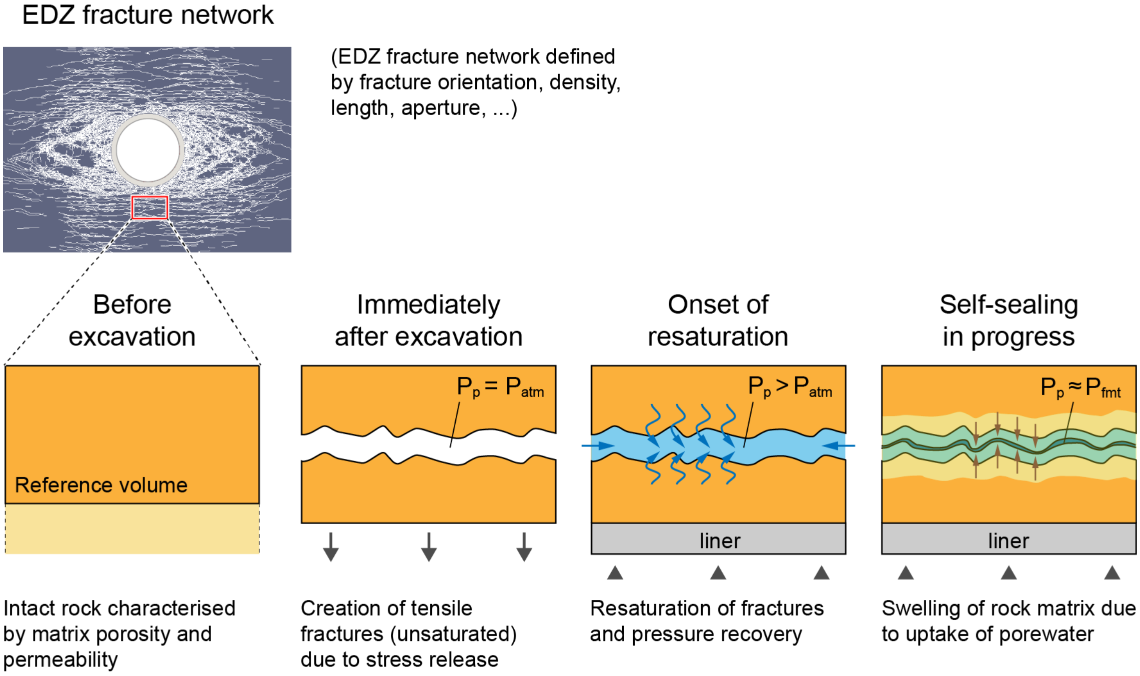

Fig. 2-1: Schematic sketch of the conceptual framework for EDZ fracture closure in Opalinus Clay, covering the key phenomena and features from the early post excavation phase until static formation pressure recovery

(P_p – pore pressure; P_{atm}: atmospheric pressure, P_{fmt}: static formation pressure)

2.2 Numerical modelling approach

Geomechanical simulations (Geomechanica 2013, 2016, 2018, 2025, Lisjak et al. 2014) provide discrete fracture networks representing the EDZ around the repository structures for a wide range of stress conditions and rock strengths. As an example, Fig. 2-2 shows the simulated fracture patterns around an L/ILW emplacement cavern at the Haberstal site for a given in-situ stress state and upper/lower bound rock strength. The aperture and slip of the fractures for the simulations are colour-coded. As observed in the plot, the region near the excavation boundary has the greatest aperture and slip. Regions of significant shear displacement are bedding parallel fractures and other fractures above/below the crown/floor at a depth of 3.6 m. There is greater simulated slip and aperture for the case of upper bound rock strength as due to the significantly less dense EDZ, there is sparse interlocking within the fractured rock mass.

Discrete fracture networks provide input for studying the hydraulic significance of the EDZ (Alcolea et al. 2014, 2016; Alcolea 2018). For this, hydraulic EDZ abstractions are derived for cylindrical tunnel cross sections in an approach consisting of the following steps (Fig. 2-3):

- The discrete fracture networks are analysed, each of them consisting of thousands of cracks (thereafter called “fractures”), characterised by crack orientation, crack length and crack aperture. A box counting approach is applied to convert the fracture networks into cell-based porosity distributions.
- An empirical porosity-permeability relationship is adopted to convert cell porosities in hydraulic conductivities.
- Cell-based porosity and conductivity distributions are converted to effective, uniform porosity / conductivity values within an annular region around the repository structure (tunnel).

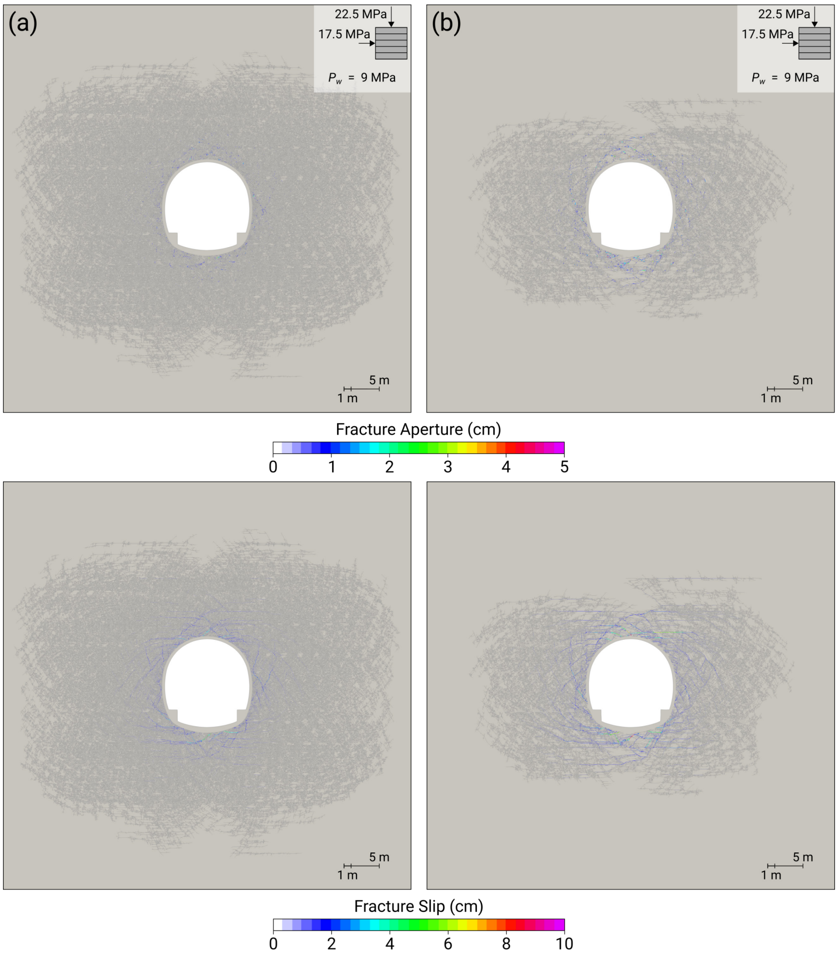

Fig. 2-2: Fracture aperture (top) and slip (bottom) contours for L/ILW cavern models with minimum horizontal in-situ stress (σ_h = 17.5 MPa) for (a) lower bound and (b) upper bound strength calibrations

The creation of the EDZ is a brittle process, i.e., the increase of the void volume in the damaged rock zone around the excavation is solely attributed to fracture opening, whereas the porosity of intact rock remains essentially unchanged during the early times after excavation. Initially, the newly created EDZ fractures are unsaturated and exposed to atmospheric pressure, whereas the intact rock remains saturated and exhibits high matrix suction as a consequence of the high gas entry pressure of the Opalinus Clay. The initial transmissivity of the unsaturated EDZ fractures is controlled by the fracture aperture and can be very high. The matrix conductivity remains essentially unchanged, i.e., it is the same as the conductivity of the intact rock. Two-phase flow scoping simulations are presented in Leupin et al. 2016a, which address the evolution of the fractured host rock around an HLW drift from the initial unsaturated state. The simulations reveal that the saturation process of the initially unsaturated pore space in the rock takes 20 – 50 years, while the buffer resaturates in a period of several hundred years. With time, the matric suction in the rock matrix decreases due to the uptake of pore-water from outer rock zones. Pore-water uptake from the intact rock zones is associated with swelling and consequently with an increase of matrix porosity. This porosity increase occurs at the expense of a decrease of fracture aperture (and correspondingly, of fracture transmissivity), i.e., fractures start to close and fracture transmissivity reduces drastically, whereas the hydraulic conductivity of the intact matrix increases slightly as a consequence of the porosity increase. The recovery of pore pressure in the rock towards static formation pressure requires more than 20,000 years. The hydraulic conductivity of the EDZ evolves with the resaturation process and pore pressure recovery. The process ends when the equilibrium of effective stresses is reached. This is essentially the case when pore pressure reaches the static formation pressure.

While the fracture transmissivities dominate the hydraulic conductance of the EDZ fracture network in the early post-closure time, pore pressure increase gives rise to progressive closure of the fractures, leading to a homogenized spatial distribution of effective porosity and effective hydraulic conductivity in the host rock around the HLW drift.

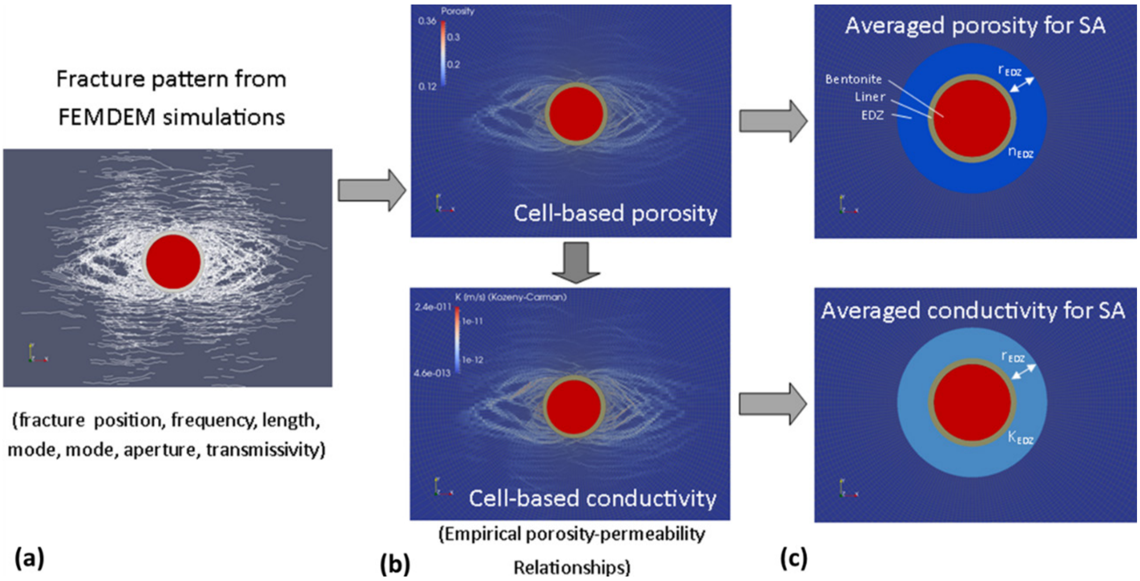

Fig. 2-3: Concept of the EDZ abstraction procedure for safety assessment (SA) applicable for a circular tunnel

After Alcolea et al. (2014):
(a) representative fracture patterns are simulated for relevant repository configurations with a discrete element model (FEMDEM). Such patterns represent the initial state of the EDZ after excavation and emplacement; (b) the discrete fracture patterns are converted to heterogeneous porosity and hydraulic conductivity distributions; (c) in a final abstraction process, the heterogeneous porosity and conductivity distributions of the EDZ are converted into a shell defined by a radius and homogeneous porosity and conductivity.

For the purpose of estimating the post-sealing hydraulic conductivity it is assumed that complete disaggregation of the Opalinus Clay has been reached in the equilibrium state, associated with swelling pressures that correspond to the swelling pressure of normally consolidated Opalinus Clay. Comprehensive laboratory tests were conducted on remoulded Opalinus Clay samples, aimed at determining hydraulic conductivity of the rock matrix under a wide range of effective stresses and the corresponding porosities in the normally consolidated state. Fig. 2-4 presents a compilation of hydraulic conductivity measurements on remoulded and recompacted Opalinus

Clay from different sites. The following power law relationship is derived (Seiphoori 2019, Nagra 2024a, Nagra 2024d), representing the dependency of hydraulic conductivity K on porosity Ø for the Opalinus Clay samples from the deep investigation boreholes in Northern Switzerland:

$$K\left[\frac{m}{s}\right] = 10^{-15} \cdot exp^{27.37 \cdot \varnothing[-]} \tag{2-1}$$

The power law-relationship is based on site specific data and substitutes previous correlations which were derived from the the Cozeny-Karman relationship (Alcolea et al. 2014).

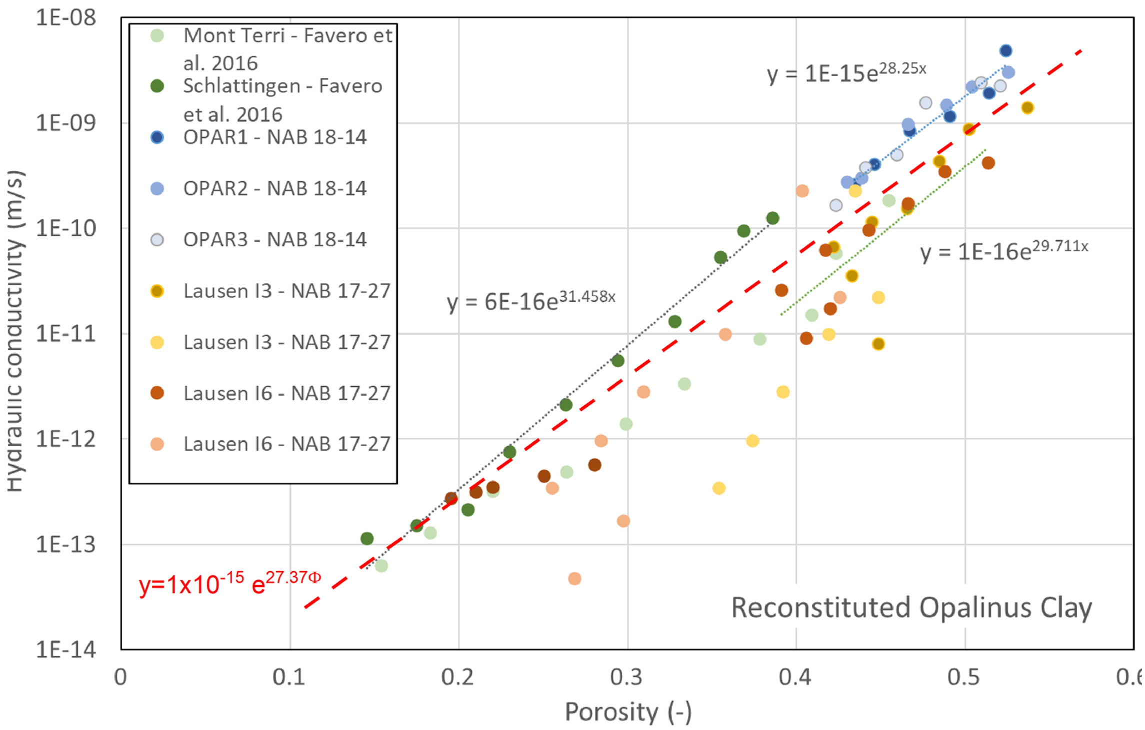

Fig. 2-4: Hydraulic conductivity measurements on remoulded and recompacted Opalinus Clay samples from various locations in Northern Switzerland

3 Results of fracture network modelling

A provisional repository project for HLW and L/ILW at the Haberstal site was elaborated in the context of the Sectoral Plan, for which the general licence application has been prepared by the end of 2024. The technical repository layout described in the engineering dossier (Nagra 2023a, Nagra 2023b) foresees the emplacement rooms for HLW and L/ILW to be placed in the Opalinus Clay formation at a depth of around 900 m.

The assessment of long-term safety of the repository requires a reliable representation of the excavation damage zone (EDZ) around the backfilled HLW and L/ILW emplacement rooms and along the shaft seals, as these can form a preferential transport path for radionuclides after repository closure. Fracture network simulations were performed by Geomechanica (2025) for the three safety-relevant repository components, namely the HLW drifts, the L/ILW caverns and the V3 shaft seals, aimed at assessing the relevance of the EDZ as a release path for dissolved and volatile radionuclides. This chapter reviews previous fracture network simulations in the context of the Sectoral Plan (Section 3.1) and summarises the results of the site specific simulations for the current repository project at the Haberstal site (Section 3.2).

3.1 Previous related numerical modelling studies

A modelling initiative was started in the framework of SGT Stage 2, aimed at evaluating repository-induced effects by numerical simulations of initiation and propagation of EDZ fractures during repository construction and their temporal evolution after backfilling of the underground structures. The results of the studies were documented in Geomechanica (2013). In particular a finite-discrete element method (FDEM) was used to simulate the discrete fracture network which develops in response to the excavation process in the rock mass around the underground structures of a radioactive waste repository. The synthetic fracture networks were then fed into a hydraulic model (Alcolea et al., 2014), aimed at providing abstracted representations of the EDZ as an input for safety analyses.

A follow-up study of the above numerical investigations was carried out with results documented in Geomechanica (2016). The report complemented the results of previous laboratory-scale models by (i) assessing the sensitivity of FEMDEM models to a variety of input parameters and boundary conditions and (ii) producing a series of characteristic plots suitable to perform continuum-based diagnostic analyses of geomechanical properties.

In preparation of SGT Stage 3, a further sensitivity study was initiated on the EDZ formation around the L/ILW and SF/HLW emplacement rooms at three candidate repository sites (Jura Ost – JO, Zürich Nordost - ZNO, Nördlich Lägern - NL). The sensitivity analysis included assessing the effect of varying the rock strength, in-situ stress field, and pore pressure on the formed EDZ. The results of the study are documented in Geomechanica (2018).

3.2 Simulation of EDZ fracture patterns – cross sections and cases

Fracture network simulations were performed by Geomechanica (2025) as a contribution to the safety case for the provisional repository project at the Haberstal site. The 2D simulations encompassed a sensitivity study on the EDZ formation around three safety-relevant repository components, namely the HLW emplacement drifts, the L/ILW emplacement caverns and the operations shaft. Nine simulations were carried out for each of the three cross-sections with varying in-situ stress, rock strength properties and lining characteristics.

The latest version of the FDEM software, Irazu V. 6.1, was used for this study (Geomechanica 2025). Starting with the calibration results from NAB 13-78 (Geomechanica 2013) and Geomechanica (2016), the Opalinus Clay strength properties were adjusted to reflect the new laboratory data by Madaschi et al. (2023). The updated input parameters were strictly a result of minor UCS calibration.

A core replacement technique was adopted to capture the supporting effect of the tunnel face in the two-dimensional FDEM model (see also Geomechanica 2025). With this technique, the three-dimensional face effect, which causes a gradual reduction of radial resistance around the excavation boundary, is captured by a fictitious, softening elastic material in the tunnel core. That is, the deformation modulus of the excavated material is progressively reduced from the original rock mass values, corresponding to an undeformed section far ahead of the face, to a value that results in the wall displacements at the time of support installation. The general procedure for modelling excavation advance and support installation in FDEM consisted of two main steps, summarized graphically in Fig. 3-1. Using the core replacement technique, the modulus reduction necessary to obtain the prescribed amount of tunnel wall displacement needs to be simulated. To this end, a FDEM simulation was run whereby the elastic parameters of the fictitious core material were reduced by a factor α_s (core softening ratio) decreasing over time (from 1 to 0), and the wall displacements recorded. The result was the plot of the tunnel wall displacements, δ, as function of α_s.

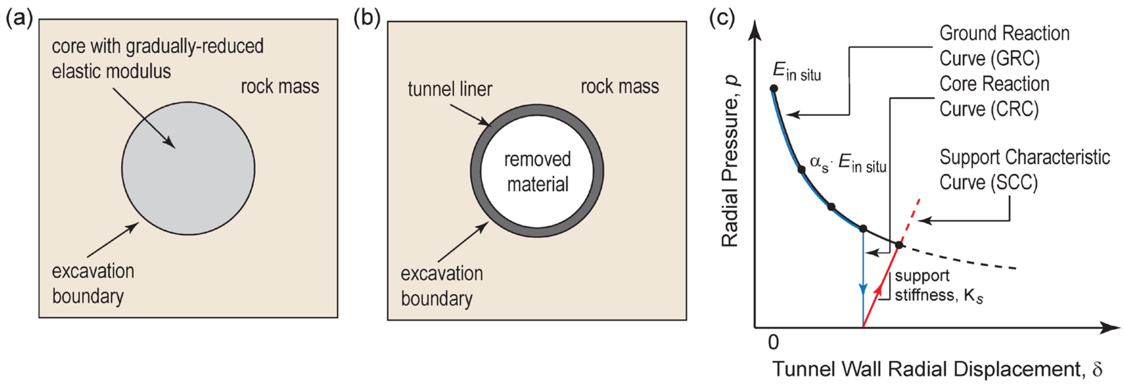

Fig. 3-1: Modelling procedure for excavation advance and support installation using the core replacement technique

(a) Replacement of core with reduced elastic modulus material. (b) Installation of tunnel lining. (c) Qualitative example of ground reaction curve simulated by modulus reduction and support characteristic curve for a linear elastic lining.

The FDEM simulation was then re-run by allowing the excavation boundary to relax up to the point where the prescribed wall displacements were obtained and by subsequently adding the support. The maximum allowed total wall closures were based on the technical repository layout described in the engineering dossier (Nagra 2023b). Ground Reaction Curves (GRC) were provided in Madaschi et al. (2023), representing the short term and long-term convergence of the crown and side wall in response to support pressure as upper / lower bounds of expected convergence for the 3 cross-sections. The maximum allowed total wall closures are 6.1 cm, 20.5 cm, and 17.2 cm for the HLW, L/ILW, and shaft excavations, which is approximately 3.3% of the radius or half the horizontal span of the L/ILW excavations (Fig. 3-2). This corresponds with the short-term sidewall convergence at zero support pressure in Fig. 3-2, additionally the short-term crown convergence (1.2%), which is 2.2 cm, 8.5 cm, and 6.2 cm for the HLW, L/ILW, and shaft excavations, was also considered in all simulation plots for comparison (further details in Geomechanica 2025).

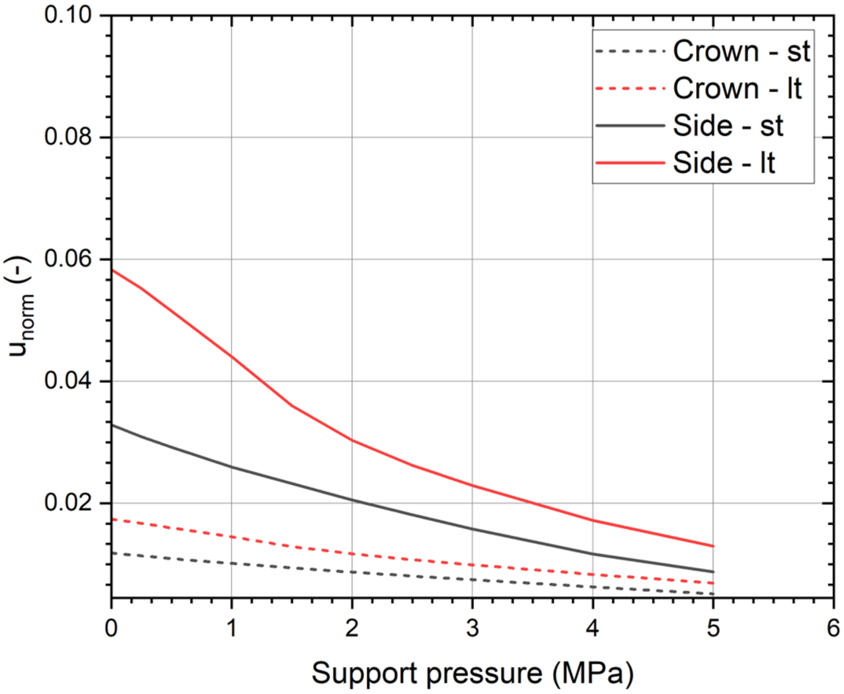

Fig. 3-2: Normalized short-term (st) and long-term (lt) ground reaction curves provided by Madaschi et al. (2023), used to determine excavation convergence before liner installation

Corresponding to the base case in Madaschi et al. 2023.

Temporal evolution of excavation wall convergence during the core modulus reduction sequence and subsequent lining activation was monitored in detail using four output history points located in the sidewalls (P_0 and P_{180}), roof (P_{90}) and floor (P_{270}) of the HLW, L/ILW, and shaft models (Fig. 3-3). Maximum allowed closure values were accounted for by examining the displacement components in the direction perpendicular to the excavation walls and allowing the excavation core material to relax up until the point in which one (or more) displacement components (in absolute terms) reached an approximate value of about 6.1 cm, 20.5 cm, and 17.2 cm, for HLW, L/ILW, and shaft models respectively. For the HLW and shaft models, due to the circular shape of the excavation, the radial displacement, δ_r, is monitored, while for the L/ILW model, the x-displacement, δ_x, is monitored for P_0 and P_{180}, while the y-displacement, δ_y, is monitored for P_{90} and P_{270}.

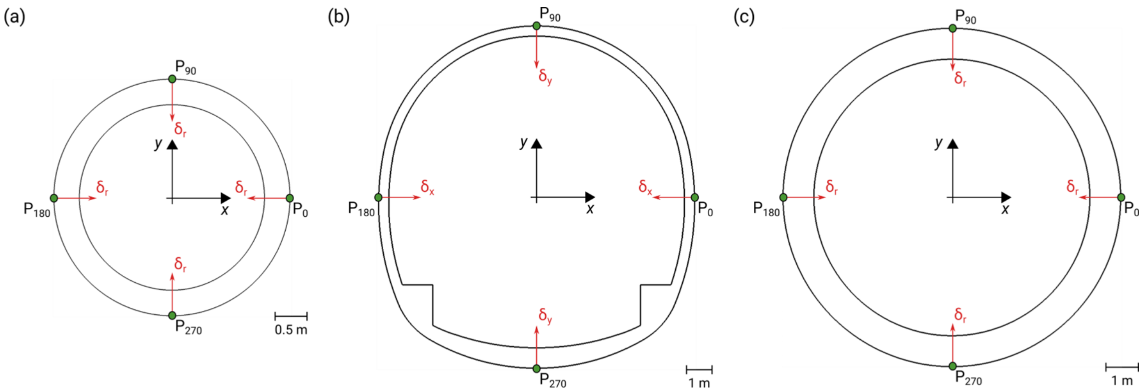

Fig. 3-3: Output history points used to monitor excavation wall displacements in the (a) HLW, (b) L/ILW, and (c) shaft models

The EDZ was simulated for 9 cases of the HLW / L-ILW emplacement rooms and for the shaft, with varying horizontal in-situ stress, rock strength, core softening ratio, and core softening scheme. For each HLW model, the core softening ratio was adjusted such that the maximum deformation at one of the four monitoring points converges approximately 6.1 cm before the liner is installed. For all models, an initial pore pressure of 9 MPa is applied to the rock mass, with the liner being prescribed zero pore pressure (see Tab. 3-1, Tab. 3-2 and Tab. 3-3).

Tab. 3-1: Summary of HLW emplacement tunnel simulations performed in this study

Case	**Total horizontal stress, σ_h** [MPa]	**Initial effective horizontal stress, σ_h'** [MPa]	**Rock strength properties** [upper/lower limit]	**Core softening scheme**	**Core softening ratio, α_s**
1	17.5	8.5	Lower limit	Isotropic	0.0025
2	17.5	8.5	Upper	Itropic	0.0010
3	22.5	13.5	Lower	Isotropic	0.0020
4	22.5	13.5	Upper	Isotropic	0.0015
5	29.25	20.25	Lower	Isotropic	0.0040
6	29.25	20.25	Upper	Isotropic	0.0030
7	29.25	20.25	Lower	Anisotropic	0.01
8	17.5	8.5	Lower	Anisotropic	0.125
9	22.5	13.5	Lower	Anisotropic	0.125

Tab. 3-2: Summary of ILW cavern simulations performed in this study

Case	Total horizontal stress, σ_h [MPa]	Initial effective horizontal stress, σ_h' [MPa]	Rock strength properties [upper/lower limit]	Core softening scheme	Core softening ratio, α_s
1	17.5	8.5	Lower limit	Isotropic	0.0025
2	17.5	8.5	Upper	Isotropic	0.001
3	22.5	13.5	Lower	Isotropic	0.003
4	22.5	13.5	Upper	Isotropic	0.00165
5	29.25	20.25	Lower	Isotropic	0.004
6	29.25	20.25	Upper	Isotropic	0.00375
7	29.25	20.25	Lower	Anisotropic	0.0133
8	17.5	8.5	Lower	Anisotropic	0.125
9	22.5	13.5	Lower	Anisotropic	0.125

Tab. 3-3: Summary of shaft simulations performed in this study

Case	Total horizontal stress, σ_h [MPa]	Initial effective horizontal stress, σ_h' [MPa]	Rock strength properties [upper/lower limit]	Core softening scheme	Core softening ratio, α_s
1	17.5	8.5	Lower limit	Isotropic	0.0004
2	17.5	8.5	Upper	Isotropic	0.0001
3	22.5	13.5	Lower	Isotropic	0.00045
4	22.5	13.5	Upper	Isotropic	0.0001
5	29.25	20.25	Lower	Isotropic	0.00095
6	29.25	20.25	Upper	Isotropic	0.0005
7	29.25	20.25	Lower	Isotropic	0.007
8	17.5	8.5	Lower	Isotropic	0.004
9	22.5	13.5	Lower	Isotropic	0.004

Exemplarily, the simulated aperture and slip of the fractures for the simulation cases HLW-1 and HLW-2 are shown in Fig. 3-4. As observed in the plot, the region near the excavation boundary has the greatest aperture and slip. Regions of significant shear displacement are bedding parallel fractures above/below the crown/floor and conjugate shear fractures in the sidewalls. The corresponding maximum and minimum principal stress contours for the simulations are shown in Fig. 3-5 and Fig. 3-6.

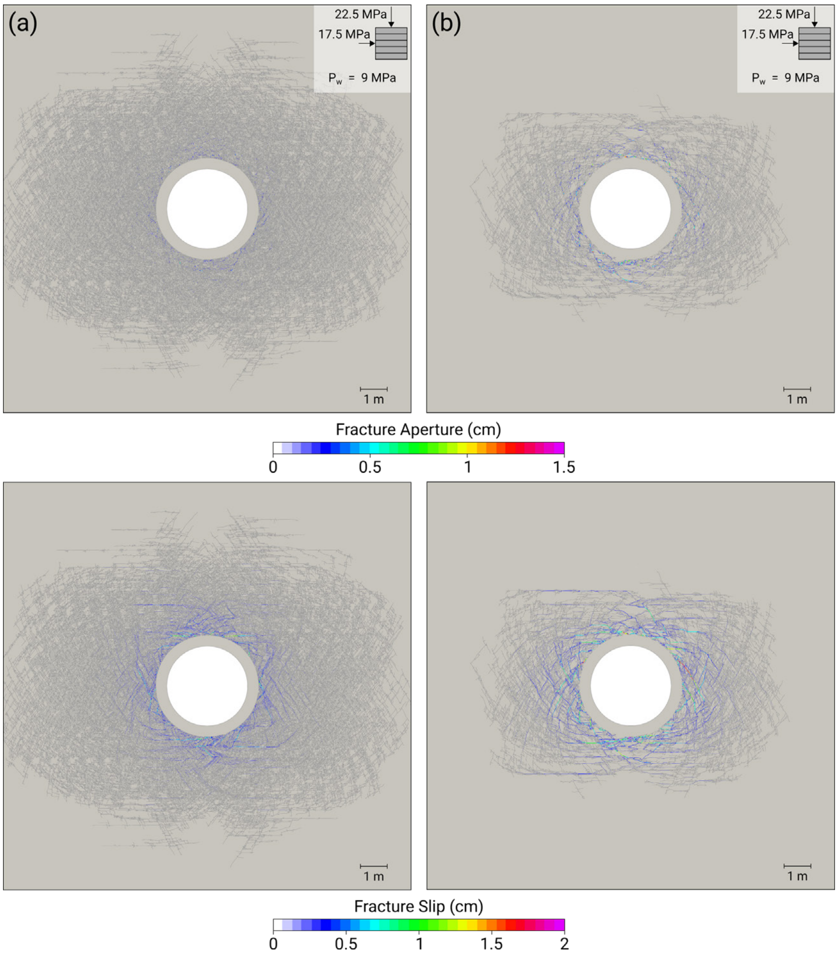

Fig. 3-4: Fracture aperture (top) and slip (bottom) contours for HLW tunnel models with minimum horizontal in-situ stress (σ_h = 17.5 MPa) for (a) lower bound and (b) upper bound strength calibrations

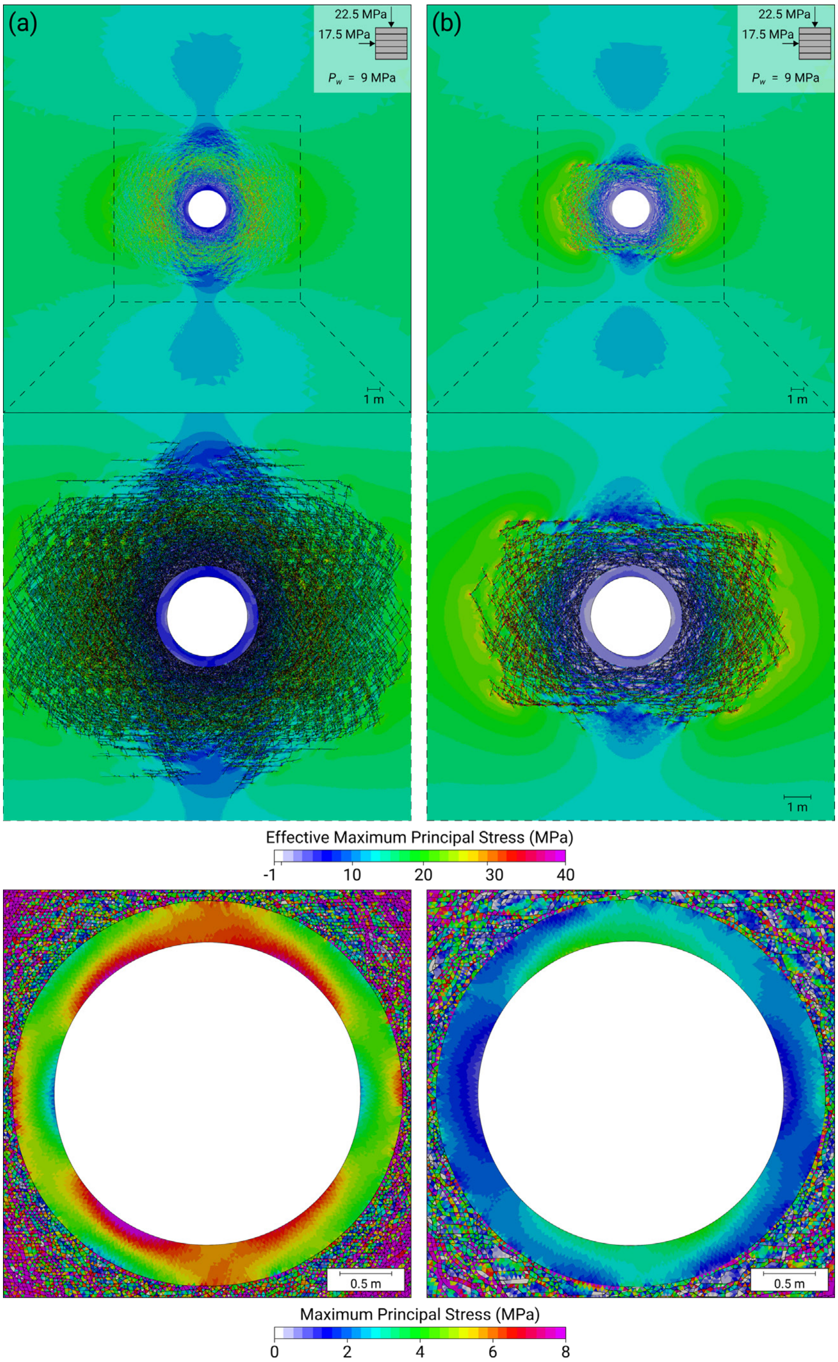

Fig. 3-5: Effective maximum principal stress (top) and maximum principal stress (bottom) contours for HLW tunnel models with minimum horizontal in-situ stress (σ_h = 17.5 MPa) for (a) lower bound and (b) upper bound strength calibrations

Positive stress is compression.

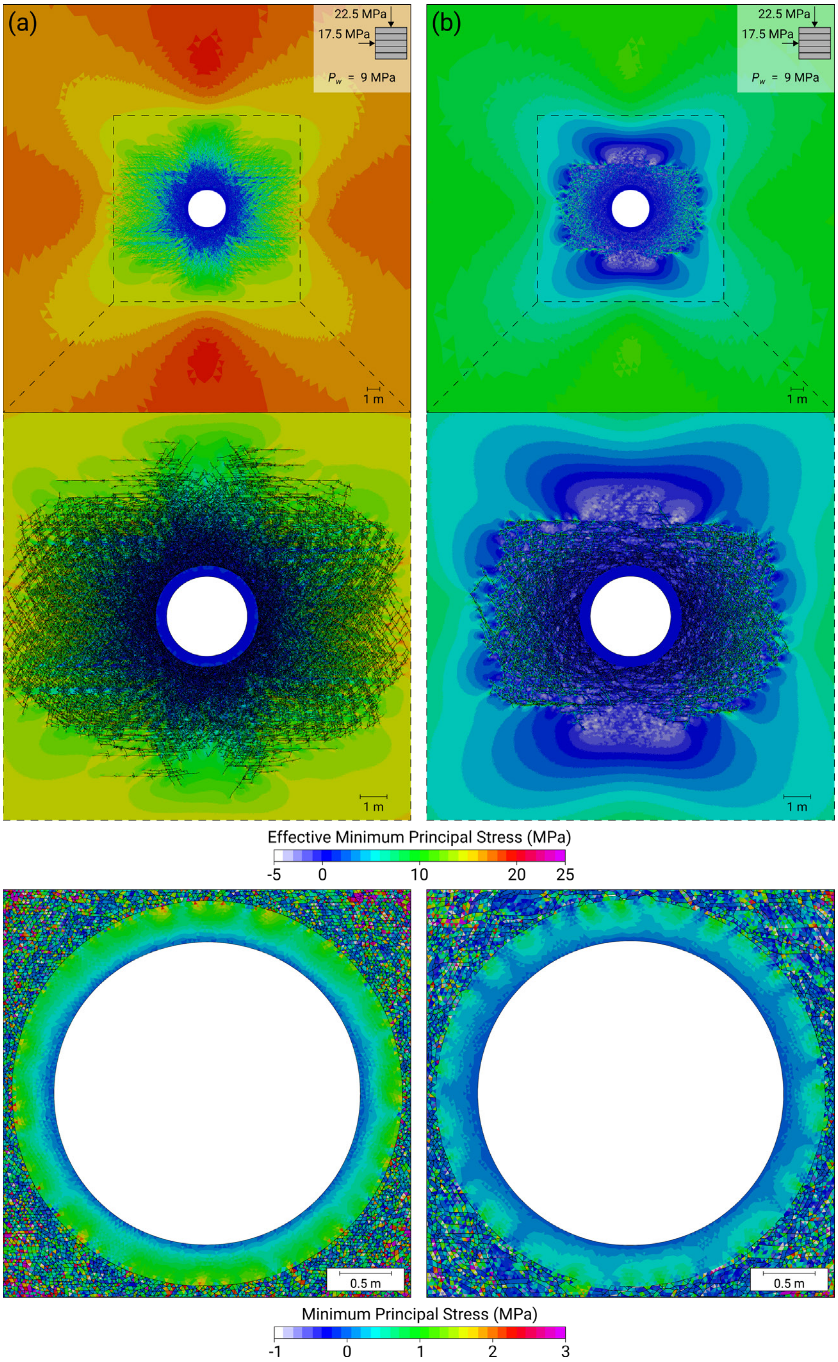

Fig. 3-6: Effective minimum principal stress (top) and minimum principal stress (bottom) contours for HLW tunnel models with minimum horizontal in-situ stress (σ_h = 17.5 MPa) for (a) lower bound and (b) upper bound strength calibrations

Positive stress is compression.

4 Calculation of effective hydraulic EDZ properties (late time properties)

The discrete fracture networks described in chapter 3 provide the geometric input for studying the hydraulic significance of the EDZ. Following the workflow which was presented in Section 2.2 (see also Fig. 2-3), cell-based porosity and hydraulic conductivity distributions are derived in Section 4.1 for the three types of cross-sections (HLW drift, L/ILW cavern and V3 seal). In a next step, the cell-based porosity and conductivity distributions are converted to effective, uniform porosity / conductivity values within an annual region around the excavation (Section 4.2). Look-up tables are calculated for each cross-section.

4.1 Cell-based porosity and hydraulic conductivity distributions

The outputs of the fracture network simulations were analysed with the numerical approach by Alcolea et al. (2014 and 2016). In this report we focus on the derivation of the late time hydraulic conductivities $K(r_i,\varphi_j)$ from cell-based porosity values $\Phi(r_i,\varphi_j)$, calculated by box counting the fracture areas (fracture area = fracture trace length × fracture aperture) for all cells of a radial-symmetric mesh, indicated by the cell coordinates r_i,φ_j (i=1,…, I; j=1,…, J):

$$\phi(\mathrm{r}_i, \varphi_j) = \frac{\sum_{k=1}^{K} fa_k}{A_{ij}} \tag{4-1}$$

where fa_k represents the fracture area of the k-th fracture in the cell {i,j} and A_{ij} is the total cell area of the cell {i,j}. The hydraulic conductivity distribution $K(r_i,\varphi_j)$ correlates with the porosity field $\Phi(r_i,\varphi_j)$ according to the power law relationship given in equation (2-1).

The next step towards an abstracted EDZ representation for PA/SA modelling consists of the conversion of the heterogeneous distributions $\Phi(r_i,\varphi_j)$ and $K(r_i,\varphi_j)$ in radial symmetric distributions of porosities $\Phi(r_i)$ and hydraulic conductivities $K(r_i)$:

$$\phi(r_i) = \frac{1}{J} \cdot \sum_{j=1}^{J} \phi(r_i, \varphi_j) \tag{4-2}$$

$$K(r_i) = \prod_{j=1}^{J} \left(K(r_i, \varphi_j)\right)^{\frac{1}{J}} \tag{4-3}$$

Note that the arithmetic mean is adopted for the porosity profiles, whereas the geometric mean is used to estimate the averaged conductivity profiles.

The total (secondary) void volume $<V_{EDZ}>$ and total axial flux $<Q_{EDZ}>$ along the EDZ (in response to a hydraulic gradient of 1) are calculated by integration:

$$< V_{EDZ} \geq \int_{r_o}^{\infty} < \phi(r) > -\phi_{matrix}) \cdot r \cdot dr \tag{4-4}$$

$$< Q_{EDZ} \geq \int_{r_o}^{\infty} < K(r) > -K_{matrix}) \cdot r \cdot dr \tag{4-5}$$

where r_o represents the radius of the unlined tunnel. Eventually, the average void volume $<V_{EDZ}>$ and the corresponding total axial flux $<Q_{EDZ}>$ (i.e., total axial flow computed under unit gradient) are used to define homogenised properties of the abstracted EDZ in terms of a relationship between the equivalent porosity / hydraulic conductivity $\phi_{EDZ,equiv}$ / $K_{EDZ,equiv}$ and the associated equivalent EDZ thickness d_{equiv}:

$$\phi_{EDZ,equiv} = \phi_{matrix} + \frac{<V_{EDZ}>}{(r_{equiv}^2 - r_0^2) \cdot \pi} \quad (4\text{-}6)$$

$$K_{EDZ,equiv} = K_{matrix} + \frac{<Q_{EDZ}>}{(r_{equiv}^2 - r_0^2) \cdot \pi} \quad (4\text{-}7)$$

where the equivalent EDZ thickness is $d_{equiv} = r_{equiv} - r_o$.

Fig. 4-1 to Fig. 4-3 display the late time distributions of hydraulic conductivity and porosity for the HLW cross-sections, Fig. 4-4 to Fig. 4-6 for the L/ILW cross-sections and Fig. 4-7 to Fig. 4-9 for shaft models, respectively.

A radial profile of equivalent hydraulic conductivity K(r) and total porosity Φ(r) is calculated for each of the 9 simulation cases. Fig. 4-10 presents the 9 radial profiles (i=1,…9) of $K_i(r)$ (left) and $\Phi_i(r)$ (right), corresponding to the three cross-sections HLW (top), L/ILW (middle) and shaft (bottom).

Finally, the averaged porosity and permeability profiles were converted into a look-up table, providing equivalent thicknesses, equivalent hydraulic conductivities and equivalent porosities of the homogenized EDZ for the HLW drifts, L/ILW caverns and for the shaft seal (Section 4.2).

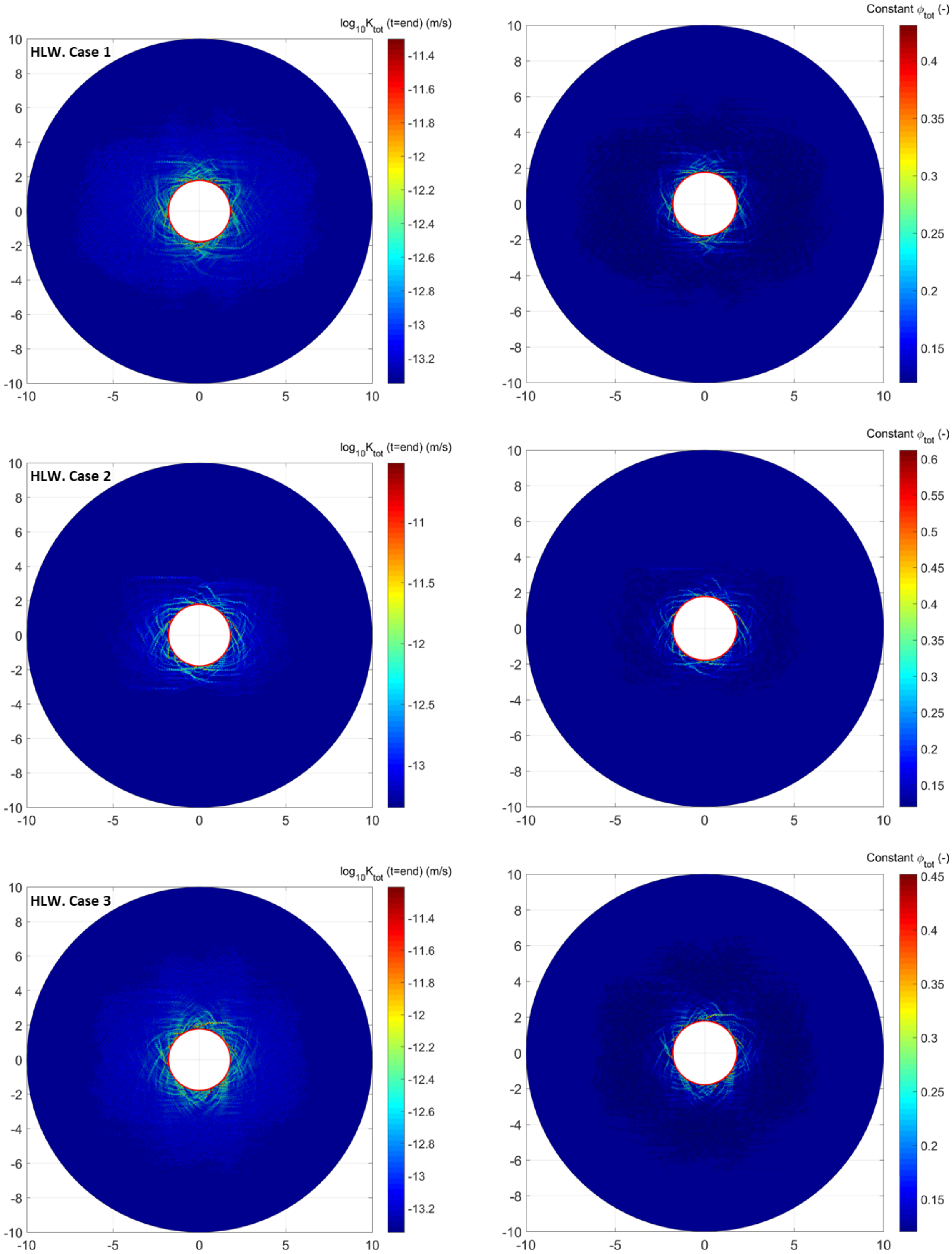

Fig. 4-1: Spatial distributions of hydraulic conductivity (left) and porosity (models) derived for fracture patterns 1 to 3 (see Tab. 3-1), corresponding to the HLW tunnels

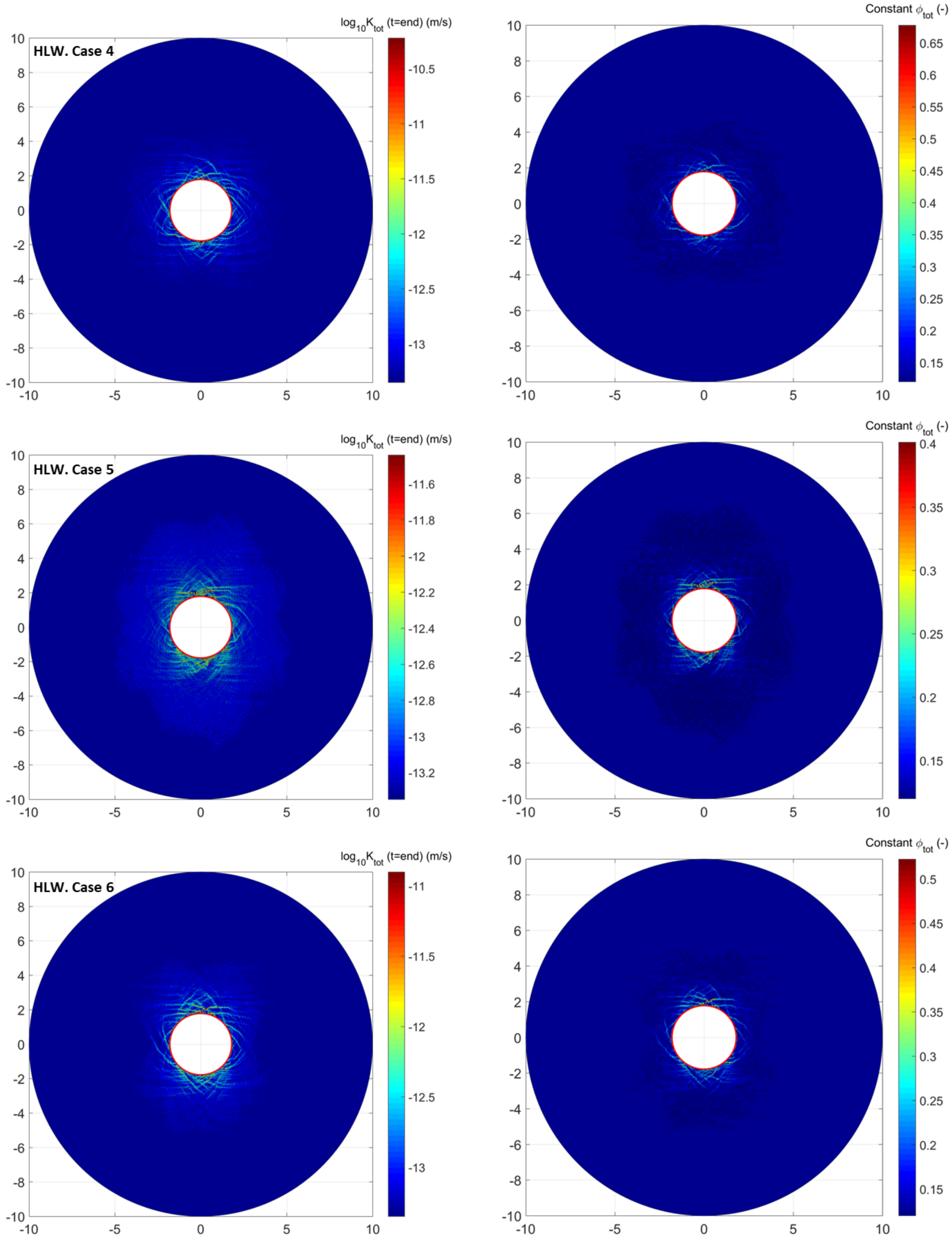

Fig. 4-2: Spatial distributions of hydraulic conductivity (left) and porosity (models) derived for fracture patterns 4 to 6 (see Tab. 3-1), corresponding to the HLW tunnels

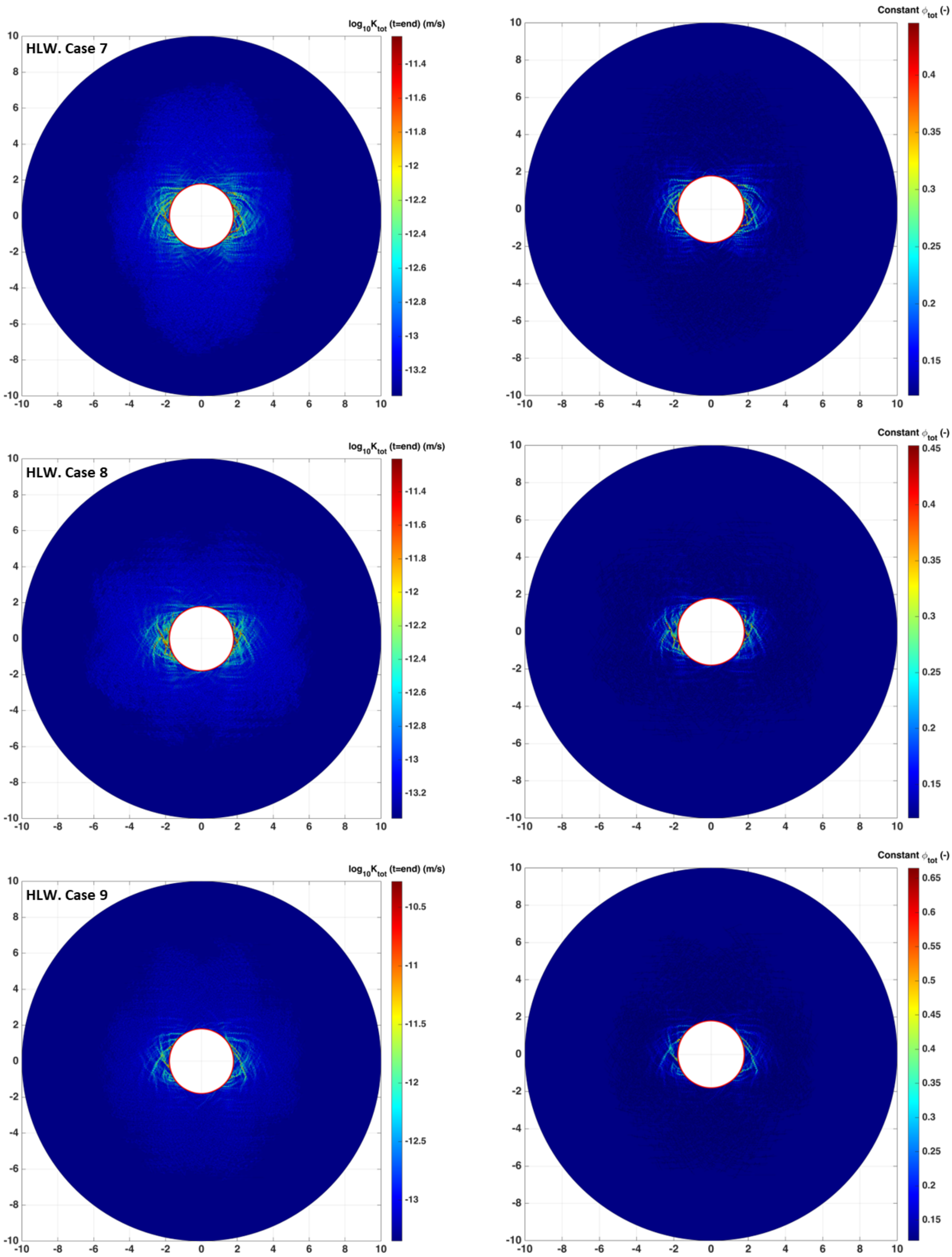

Fig. 4-3: Spatial distributions of hydraulic conductivity (left) and porosity (models) derived for fracture patterns 7 to 9 (see Tab. 3-1), corresponding to the HLW tunnels

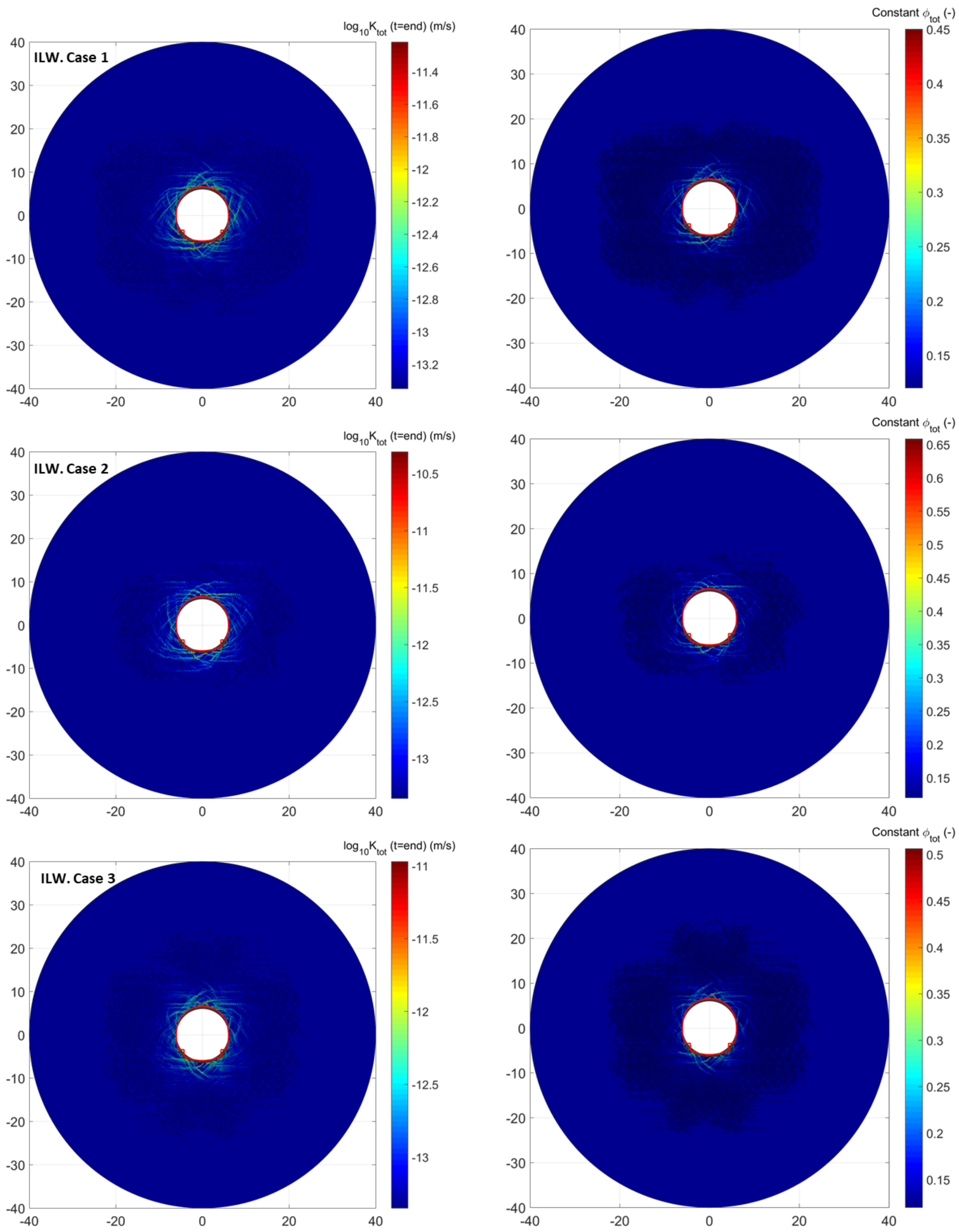

Fig. 4-4: Spatial distributions of hydraulic conductivity (left) and porosity (models) derived for fracture patterns 1 to 3 (see Tab. 3-2), corresponding to the ILW tunnels

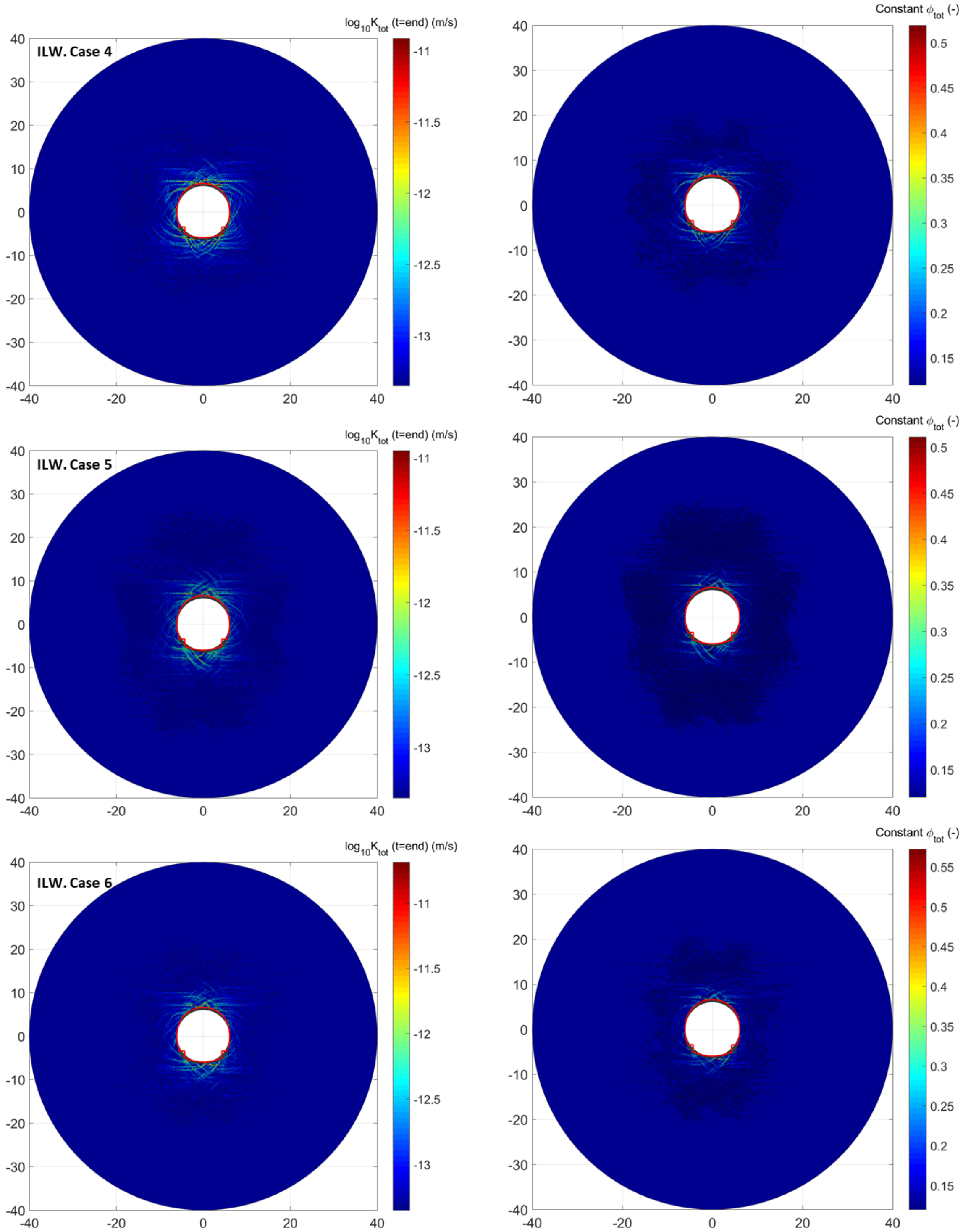

Fig. 4-5: Spatial distributions of hydraulic conductivity (left) and porosity (models) derived for fracture patterns 4 to 6 (see Tab. 3-2), corresponding to the ILW tunnels

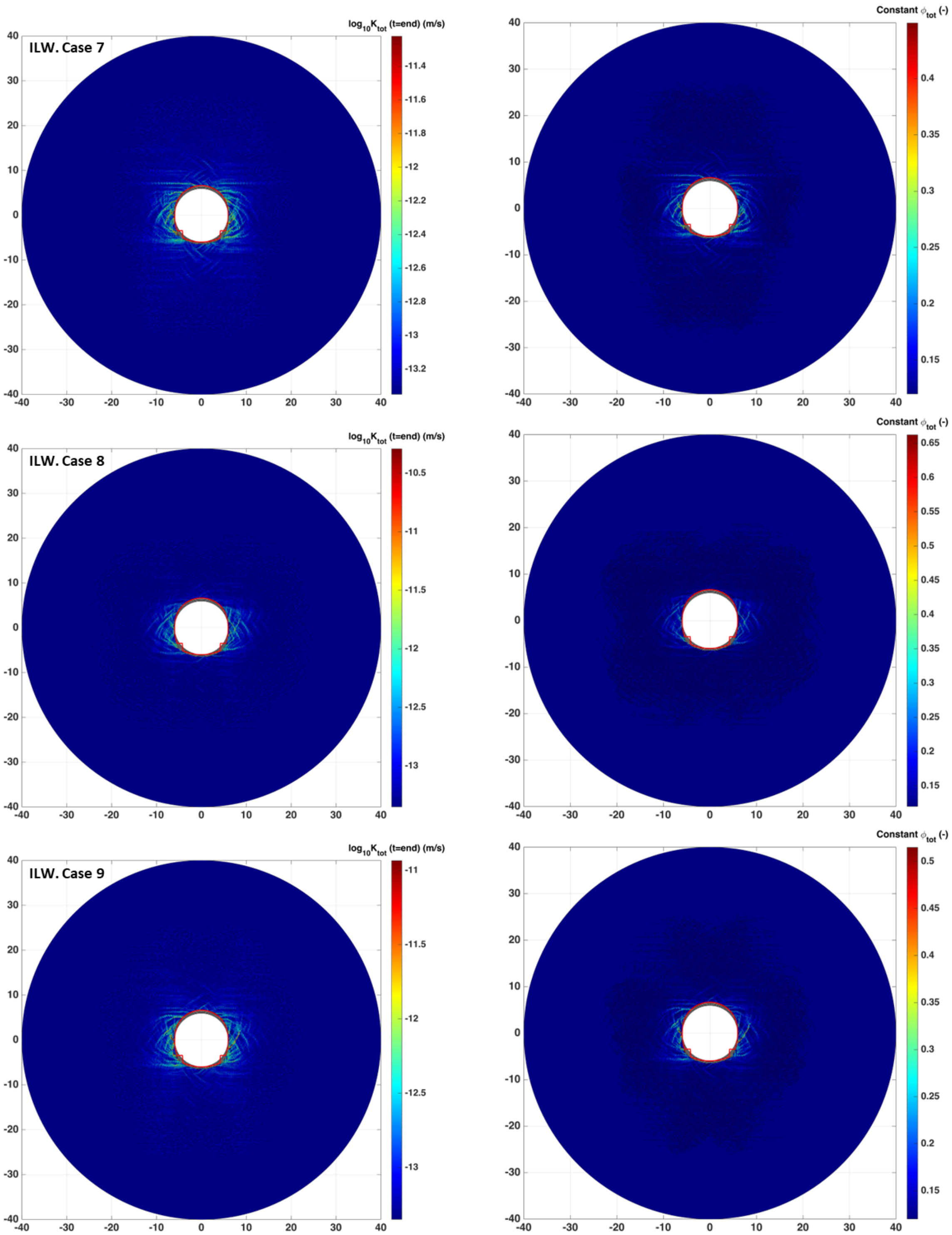

Fig. 4-6: Spatial distributions of hydraulic conductivity (left) and porosity (models) derived for fracture patterns 7 to 9 (see Tab. 3-2), corresponding to the ILW tunnels

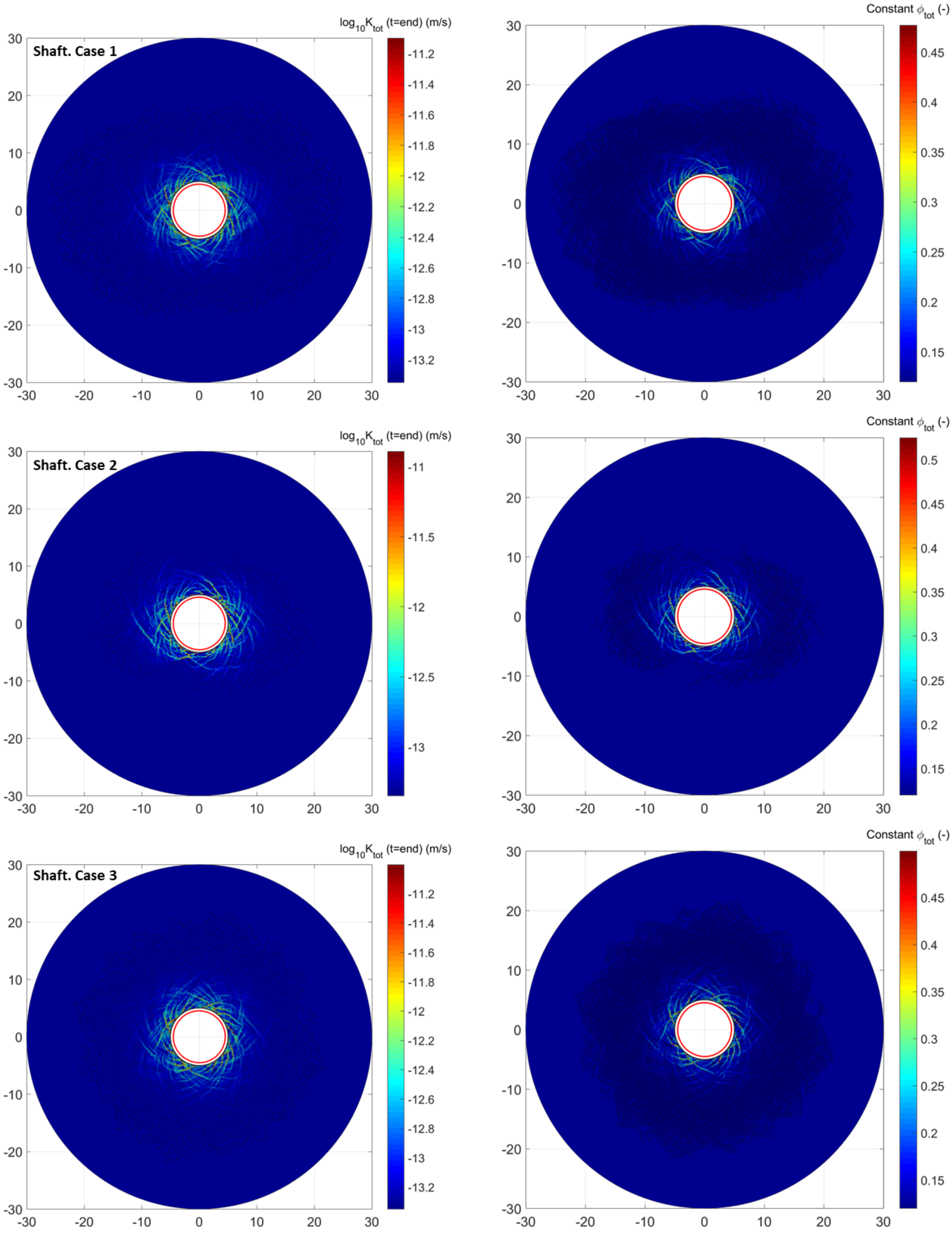

Fig. 4-7: Spatial distributions of hydraulic conductivity (left) and porosity (models) derived for fracture patterns 1 to 3 (see Tab. 3-3), corresponding to the shafts

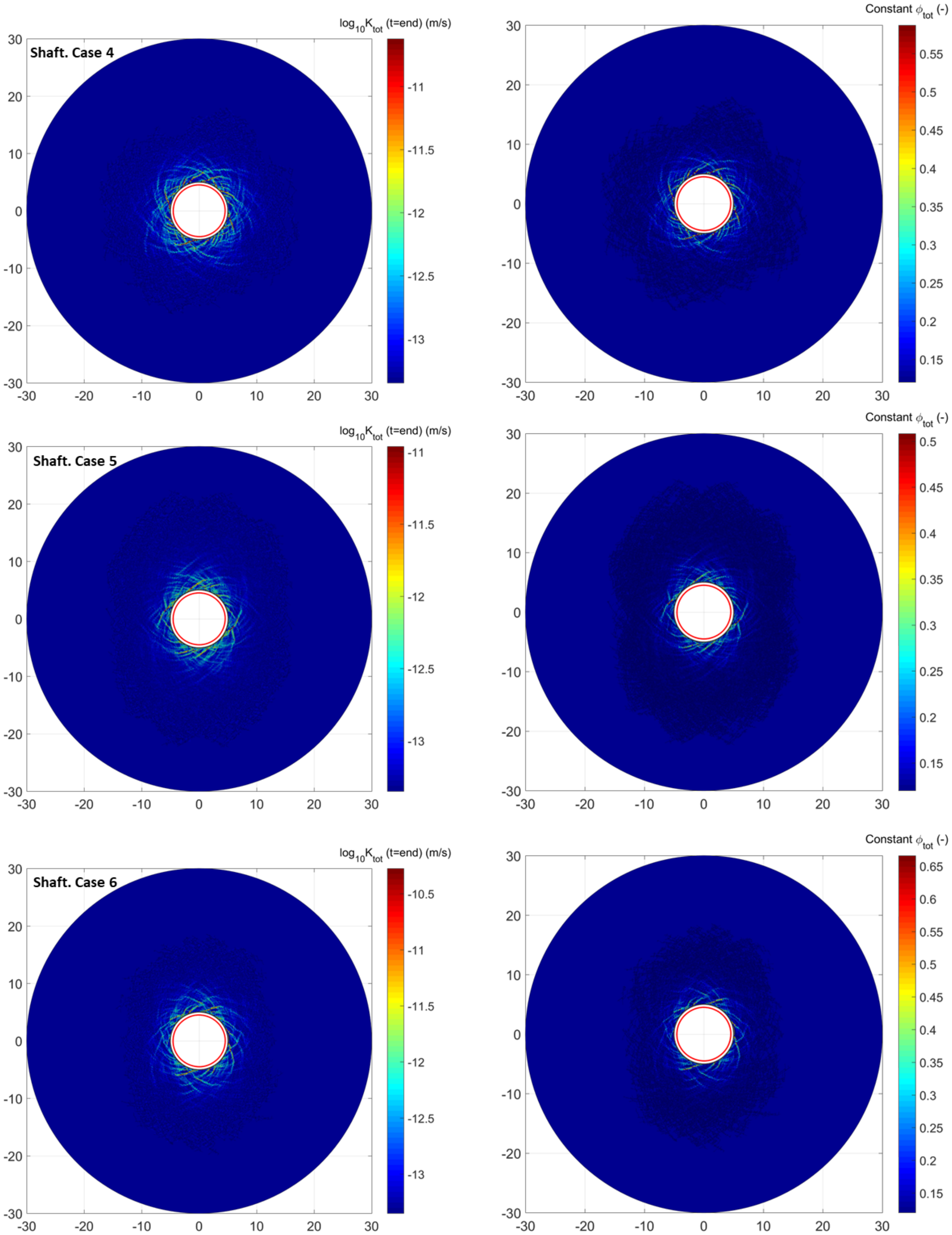

Fig. 4-8: Spatial distributions of hydraulic conductivity (left) and porosity (models) derived for fracture patterns 4 to 6 (see Tab. 3-3), corresponding to the shafts

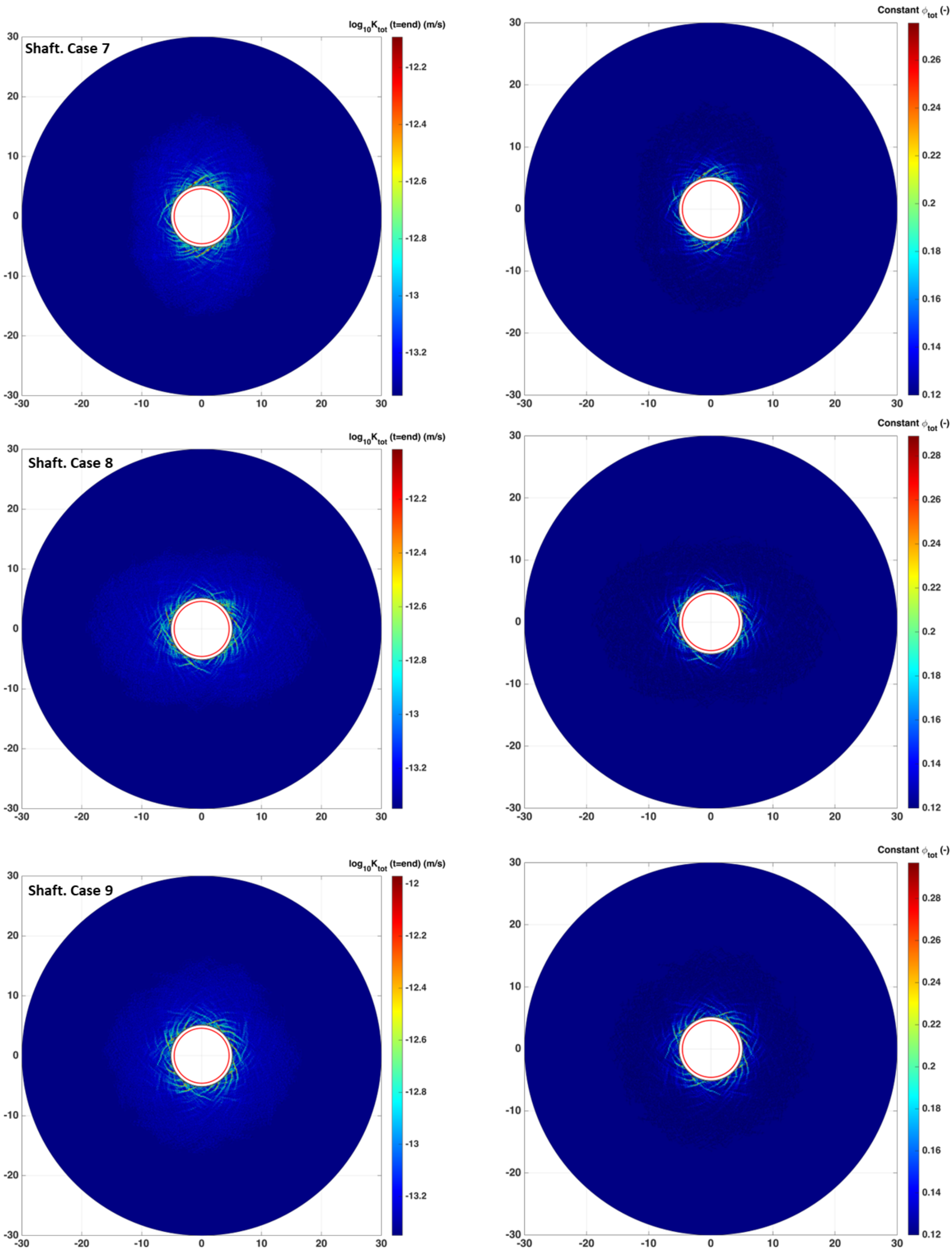

Fig. 4-9: Spatial distributions of hydraulic conductivity (left) and porosity (models) derived for fracture patterns 7 to 9 (see Tab. 3-3), corresponding to the shafts

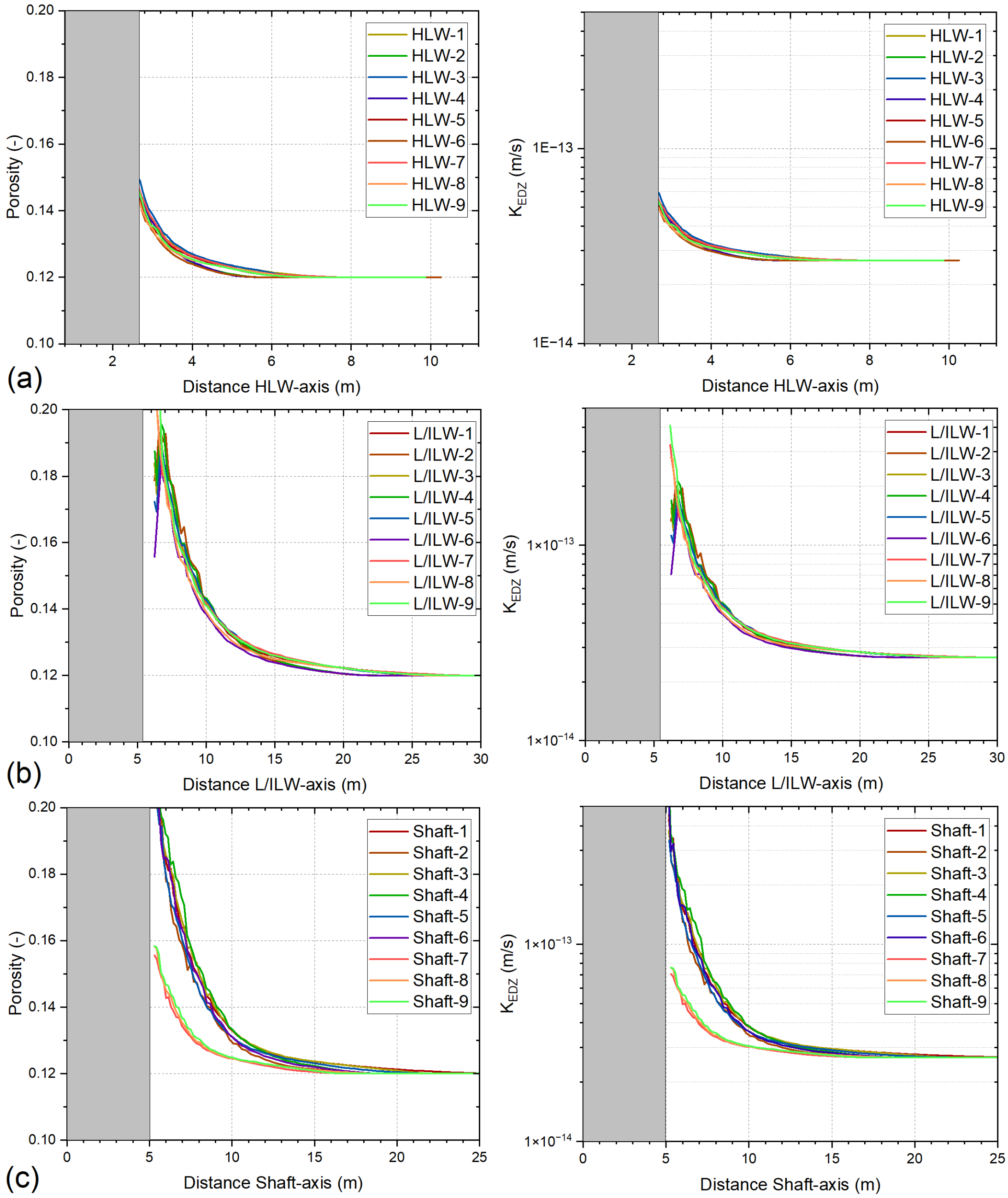

Fig. 4-10: Radial profiles of equivalent porosity (left column) and hydraulic conductivity (right, semi-log plot) according to equations (4-2) and (4-3) derived from the 2D spatial distributions of hydraulic conductivity and porosity (Fig. 4-1 to Fig. 4-9): HLW tunnels (top), L/ILW caverns (middle) and shaft (lower)

4.2 Derivation of EDZ radial profiles

Finally, the radial porosity and permeability profiles were converted according to equations (4-6) and (4-7) into equivalent thicknesses, equivalent hydraulic conductivities and equivalent porosities of the homogenized EDZ for the HLW drifts, L/ILW caverns and for the shaft, forming the inputs for the dose calculations. The graphical representation of the homogenised porosities and conductivities are given in Fig. 4-11.

Despite the significant differences between the analysed EDZ fracture networks, the differences between the nine profiles of equivalent (homogenized) porosity and hydraulic conductivity are relatively small, justifying a simple averaging of the profiles for the three cross sections:

$$< \phi(r_{equiv}) >= \frac{1}{9} \cdot \sum_{i=1}^{9} \phi_{EDZ,equiv}(r_{equiv}) \tag{4-8}$$

$$< K(r_{equiv}) > = \prod_{i=1}^{9} \left(K_i(r_{equiv})\right)^{\frac{1}{9}} \tag{4-9}$$

The averaged profiles of equivalent (homogenised) porosity and hydraulic conductivity are tabulated in the look up table given in Tab. 4-1.

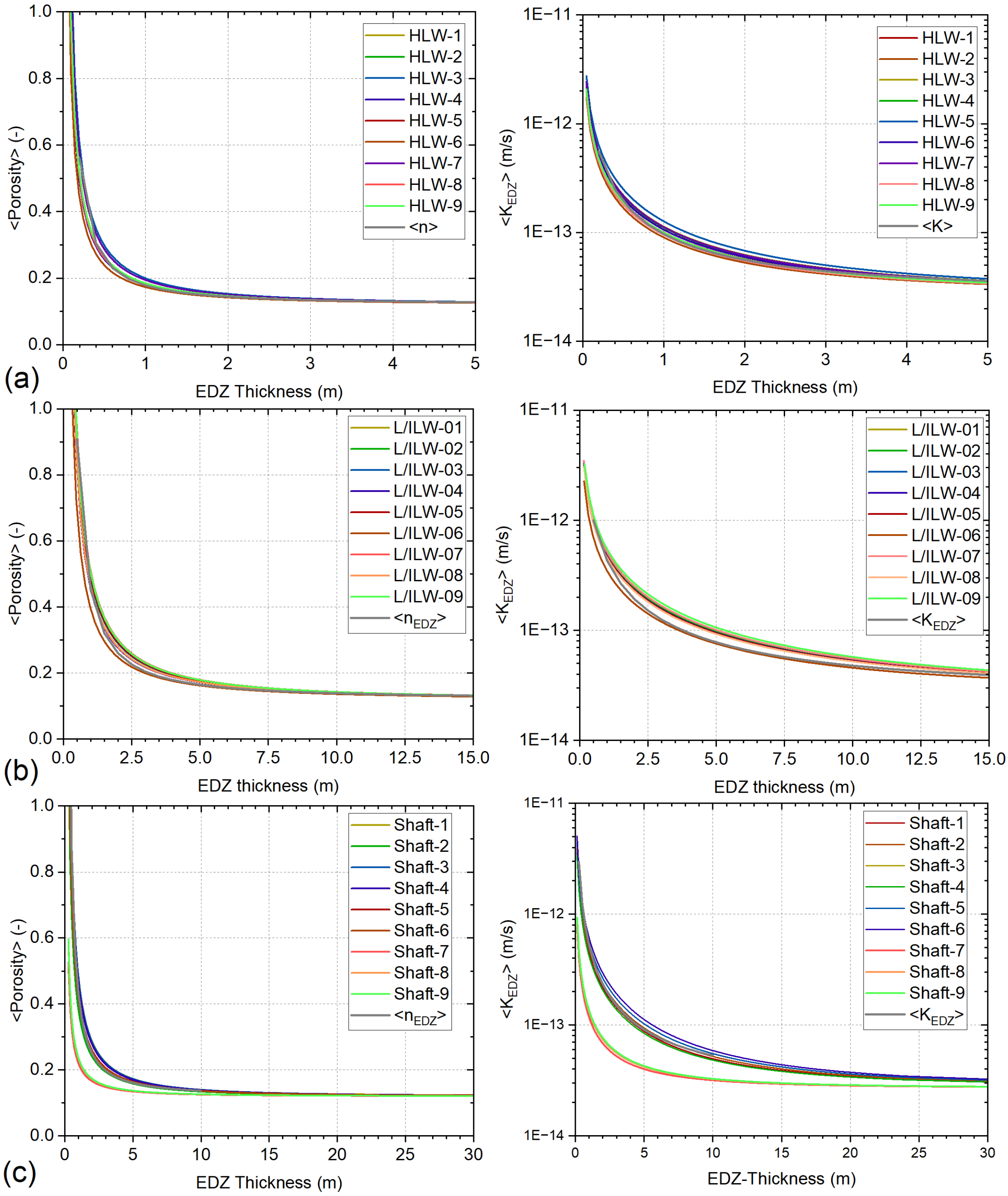

Fig. 4-11: Radial profiles of homogenised porosity $\Phi(r_{EDZ,equiv})$ hydraulic conductivity $K(r_{EDZ,equiv})$ derived from equations (4-6) and (4-7): HLW tunnels (a), L/ILW caverns (b) and shaft (c)

Note that unphysical porosity values > 1 are derived when $d_{equiv} << r_o$.

Tab. 4-1: Look-up tables representing thickness d_{equiv}, equivalent hydraulic conductivity $<K_{equiv}>$ and equivalent porosity $<\Phi_{equiv}>$ of the homogenized EDZ of the HLW drifts, L/ILW caverns and for the V3 shaft seals

HLW drifts			**L/1LW cavernst**			**Shaft**		
Thickness [m]	$<K_{equiv}>$ [m^2/s]	$<\Phi_{equiv}>$ [-]	**Thickness**	$<K_{equiv}>$ [m^2/s]	$<\Phi_{equiv}>$ [-]	**Thickness**	$<K_{equiv}>$ [m^2/s]	$<\Phi_{equiv}>$ [-]
0.2	5.6E-13	0.560	0.5	1.0E-12	0.908	0.25	3.0E-12	1.918
0.4	2.5E-13	0.304	1.0	4.3E-13	0.452	0.50	1.2E-12	0.870
0.6	1.6E-13	0.230	1.5	2.6E-13	0.320	0.75	7.5E-13	0.569
0.8	1.2E-13	0.197	2.0	1.9E-13	0.260	1.00	5.3E-13	0.433
1.0	9.7E-14	0.178	2.5	1.5E-13	0.226	1.25	4.0E-13	0.356
1.2	8.2E-14	0.166	3.0	1.2E-13	0.204	1.50	3.2E-13	0.307
1.4	7.3E-14	0.158	3.5	1.1E-13	0.189	1.75	2.7E-13	0.274
1.6	6.5E-14	0.152	4.0	9.5E-14	0.179	2.00	2.3E-13	0.250
1.8	6.0E-14	0.148	4.5	8.5E-14	0.171	2.25	2.0E-13	0.232
2.0	5.6E-14	0.144	5.0	7.8E-14	0.165	2.50	1.8E-13	0.218
2.2	5.3E-14	0.142	5.5	7.2E-14	0.160	2.75	1.6E-13	0.207
2.4	5.0E-14	0.139	6.0	6.7E-14	0.155	3.00	1.5E-13	0.198
2.6	4.8E-14	0.137	6.5	6.3E-14	0.152	3.25	1.4E-13	0.191
2.8	4.6E-14	0.136	7.0	6.0E-14	0.149	3.50	1.3E-13	0.184
3.0	4.4E-14	0.135	7.5	5.7E-14	0.147	3.75	1.2E-13	0.179
3.2	4.3E-14	0.133	8.0	5.5E-14	0.145	4.00	1.1E-13	0.174
3.4	4.2E-14	0.132	8.5	5.3E-14	0.143	4.25	1.1E-13	0.170
3.6	4.1E-14	0.132	9.0	5.1E-14	0.141	4.50	1.0E-13	0.167
3.8	4.0E-14	0.131	9.5	4.9E-14	0.140	4.75	9.5E-14	0.164
4.0	3.9E-14	0.130	10.0	4.8E-14	0.139	5.00	9.1E-14	0.161
4.2	3.8E-14	0.130	10.5	4.6E-14	0.138	5.25	8.7E-14	0.159
4.4	3.8E-14	0.129	11.0	4.5E-14	0.137	5.50	8.3E-14	0.156
4.6	3.7E-14	0.129	11.5	4.4E-14	0.136	5.75	8.0E-14	0.154
4.8	3.6E-14	0.128	12.0	4.3E-14	0.135	6.00	7.7E-14	0.153
5.0	3.6E-14	0.128	12.5	4.3E-14	0.134	6.25	7.5E-14	0.151
5.2	3.5E-14	0.127	13.0	4.2E-14	0.134	6.50	7.2E-14	0.149
5.4	3.5E-14	0.127	13.5	4.1E-14	0.133	6.75	7.0E-14	0.148
5.6	3.5E-14	0.127	14.0	4.0E-14	0.132	7.00	6.8E-14	0.147

Tab. 4-1: Cont.

HLW drifts			**L/1LW cavernst**			**Shaft**		
Thickness [m]	$<K_{equiv}>$ [m^2/s]	$<\Phi>_{equiv}$ [-]	**Thickness** [m]	$<K_{equiv}>$ [m^2/s]	$<\Phi_{equiv}>$ [-]	**Thickness** [m]	$<K_{equiv}>$ [m^2/s]	$<\Phi_{equiv}>$ [-]
5.8	3.4E-14	0.126	14.5	4.0E-14	0.132	7.25	6.7E-14	0.146
6.0	3.4E-14	0.126	15.0	3.9E-14	0.131	7.50	6.5E-14	0.145
6.2	3.4E-14	0.126	15.5	3.9E-14	0.131	7.75	6.3E-14	0.144
6.4	3.3E-14	0.126	16.0	3.8E-14	0.130	8.00	6.2E-14	0.143
6.6	3.3E-14	0.125	16.5	3.8E-14	0.130	8.25	6.0E-14	0.142
6.8	3.3E-14	0.125	17.0	3.7E-14	0.130	8.50	5.9E-14	0.141
7.0	3.3E-14	0.125	17.5	3.7E-14	0.129	8.75	5.8E-14	0.140
7.2	3.3E-14	0.125	18.0	3.7E-14	0.129	9.00	5.7E-14	0.140
7.4	3.2E-14	0.125	18.5	3.6E-14	0.129	9.25	5.6E-14	0.139
7.6	3.2E-14	0.125	19.0	3.6E-14	0.128	9.50	5.5E-14	0.138
7.8	3.2E-14	0.124	19.5	3.6E-14	0.128	9.75	5.4E-14	0.138
8.0	3.2E-14	0.124	20.0	3.5E-14	0.128	10.00	5.3E-14	0.137

5 Summary and conclusions

The EDZ around the backfilled underground structures of a geological repository represents a viable release path for radionuclides dissolved in the porewater of the repository nearfield as well as a possible escape route for corrosion and degradation gases. The efficiency of this release path depends on the shape and extent of the EDZ and on its effective hydraulic conductance (cross-sectional area of the EDZ × effective hydraulic conductivity). Thickness and effective hydraulic conductivity of the EDZ are key parameters in performance assessment and safety assessment modelling.

This report provides the estimated hydraulic properties of the EDZ around three safety-relevant repository components, namely the HLW drifts, the L/ILW caverns and the V3 shaft seals. It is based on fracture network simulations for the provisional repository project at the Haberstal site with the technical repository layout described in the engineering dossier. Following a well-established modelling workflow, the discrete EDZ fracture networks are converted into hydraulic continuum models with heterogeneous distributions of porosity and hydraulic conductivity. In a final step, the complex shape of the EDZ is abstracted towards a simplified representation, amenable to be handled with conventional PA/SA modelling tools.

For each of the three repository components, six different EDZ fracture patterns were analysed, representing sensible EDZ realisations for a wide range of possible stress conditions at repository level. Look-up tables were generated, displaying thickness, equivalent hydraulic conductivity and equivalent porosity of the homogenized EDZ for the HLW drifts, the L/ILW caverns and the shaft seals as input for the PA/SA calculations.

6 References

Alcolea, A., Kuhlmann U., Lanyon, G.W. & Marschall, P. (2014): Hydraulic conductance of the EDZ around underground structures of a geological repository for radioactive waste – A sensitivity study for the candidate host rocks in the proposed siting regions in Northern Switzerland. Nagra Arbeitsbericht NAB 13- 94.

Alcolea, A., Kuhlmann, U., Marschall, P., Lisjak, A., Grasselli, G., Mahabadi, O., de La Vaissière, R., Leung, H. & Shao H. (2016): A pragmatic approach to abstract the EDZ around tunnels of a geological radioactive waste repository. Application to the HG-A experiment in Mont Terri. In: Norris, S., Bruno, J., Van Geet, M. & Verhoef, E. (eds) Radioactive Waste Confinement: Clays in Natural and Engineered Barriers. Geological Society, London, Special Publications, 443, http://doi.org/10.1144/SP443.8.

Alcolea, A. (2018): Hydraulic significance of the EDZ around underground structures of a geological repository for radioactive waste A sensitivity study for the repository configurations L/ILW and SF/HLW in the siting regions JO, NL and ZNO. Nagra Arbeitsbericht NAB 18-17.

BFE (2008): Sachplan Geologische Tiefenlager: Konzeptteil. BFE 2. April 2008 (Revision vom 30. November 2011). Departement für Umwelt, Verkehr, Energie und Kommunikation UVEK, Bern.

Geomechanica (2013): Extent and shape of the EDZ around underground structures of a geological repository for radioactive waste – A sensitivity study for the candidate host rocks in the proposed siting regions in Northern Switzerland. Nagra Arbeitsbericht NAB 13-78.

Geomechanica (2016): Extent and shape of the EDZ around underground structures of a geological repository for radioactive waste – Complementary studies. Nagra Arbeitsbericht NAB 16-01.

Geomechanica (2018): Extent and shape of the EDZ around underground structures of a geological repository for radioactive waste – A sensitivity study for the repository configurations L/ILW and SF/HLW in the siting regions JO, NL and ZNO. Nagra Arbeitsbericht NAB 18-12.

Geomechanica (2025): Simulation of EDZ fracture patterns around the HLW- and L/ILW-emplacement rooms of a deep geological repository in the siting region NL. Nagra Arbeitsbericht NAB 25-02.

Lanyon, G.W., Martin, D., Giger, S. & Marschall, P. (2014): Development and evolution of the Excavation Damaged Zone (EDZ) in the Opalinus Clay – A synopsis of the state of knowledge from Mont Terri. Nagra Arbeitsbericht NAB 14-87.

Leupin, O.X., Smith, P., Marschall, P., Johnson, L., Savage, D., Cloet, V., Schneider, J. & Senger, R.K. (2016a): High-level waste repository-induced effects. Nagra Technical Report NTB 14-13.

Leupin, O.X., Smith, P.A., Marschall, P., Johnson, L., Savage, D., Cloet, V., Schneider, J. & Senger, R.K. (2016b): Low- and intermediate-level waste repository-induced effects. Nagra Technical Report NTB 14-14.

Levasseur, S., Collin, F., Daniels, K., Dymitrowska, M., Harrington J., Jacops E., Kolditz O., Marschall, P., Norris, S., Sillen, X., Talandier, J., Truche, L. & Wendling, J. (2021): Initial state-of-the-art on gas transport in clayey materials. Deliverable D6.1 of the HORIZON 2020 project EURAD. EC Grant agreement no: 847593.

Levasseur, S., Collin, F., Dymitrowska, M., Harrington, J., Jacops, E., Kolditz, O., Marschall, P., Norris, S., Sillen, X., Talandier, J., Truche, L. & Wendling, J. (2023): State of the art on gas transport in clayey materials – Update. Deliverable D6.2 of the HORIZON 2020 project EURAD, Work Package Gas EC Grant agreement no: 847593.

Lisjak, A., Grasselli, G. & Vietor, T. (2014): Continuum–discontinuum analysis of failure mechanisms around unsupported circular excavations in anisotropic clay shales. International Journal of Rock Mechanics and Mining Sciences 65, pp 96-115.

Madaschi, A., Leuthold, J., Cantieni, L., & Laloui, L. (2023): Comparative numerical calculations in the context of tunnel design for nuclear waste repositories in Opalinus Clay. In T.A. Konte S. Taborda D. M. G. Zdravković L. (Ed.), Proceedings 10th NUMGE 2023: 10th European Conference on Numerical Methods in Geotechnical Engineering. https://doi.org/10.53243/NUMGE2023-127

Marschall, P., Giger, S., De La Vassière, R., Shao, H., Leung, H., Nussbaum, C., Trick, T., Lanyon, B., Senger, R., Lisjak, A. & Alcolea, A. (2017): Hydro-mechanical evolution of the EDZ as transport path for radionuclides and gas: insights from the Mont Terri rock laboratory (Switzerland). Swiss J Geosci (2017) 110:173-194.

Nagra (2014): SGT Etappe 2: Vorschlag weiter zu untersuchender geologischer Standortgebiete mit zugehörigen Standortarealen für die Oberflächenanlage: Geologische Grundlagen – Dossier IV: Geomechanische Unterlagen. Nagra Technischer Bericht NTB 14-02 Dossier IV.

Nagra (2023a): Bautechnisches Dossier. Nagra Arbeitsbericht NAB 23-01 Band 1 – 9.

Nagra (2023b): Bautechnisches Dossier Standortvergleich – Band 8: Tunnelstatik. Nagra Arbeitsbericht NAB 23-01 Band 8.

Nagra (2024a): Synthesis of the Performance Assessment for a Deep Geological Repository for Radioactive Waste. Nagra Technical Report NTB 24-22.

Nagra (2024b): Model-Based Performance Assessment for a Combined Repository. Nagra Arbeitsbericht NAB 24-25.

Nagra (2024c): Radiological Consequence Analysis for a Deep Geological Repository in Northern Switzerland. Nagra Technical Report NTB 24-18.

Nagra (2024d): Geological Properties of the Jura Ost, Nördlich Lägern and Zürich Nordost Siting Regions for Safety Assessment. Nagra Arbeitsbericht NAB 24-10.

Seiphoori, A. (2019): The effects of burial diagenesis on Opalinus clay behavior: a multiscale study of the pore structure and mechanical properties. Nagra Arbeitsbericht NAB 19-06.

App. A Processing of fracture network simulations

All fracture network simulations and the corresponding data processing presented in this report have been stored electronically in Nagra's data archive.

The folder No. together with complementary information concerning the fracture network simulation cases are given in Tab. A-1 (No. 1-9: HLW drifts; No. 10-18: L/ILW-caverns; No. 19-27: Shaft seals).

At each folder, the following files (grouped by file type) are found:

- png graphics (see also Tab. A-2)
- Abstraction_EDZ_end.txt
- Abstraction_EDZ_ini.txt
- AllFractures_Stats.out
- Equiv_K_Phi_q.xlsx
- FEMDEM.vtk
- GridProps.vtk
- Liner.vtk
- meshparams.dat
- Mode1Fractures_Stats.out
- Mode2Fractures_Stats.out
- params.dat
- shaft_min_h_low_str_CSR_0.0004_aniso_core_liner_init_P_K_5e7_add_CMR_stages_femdem.r2m_broken_joint_1550000.vtu
- shaft_min_h_low_str_CSR_0.0004_broken_joint_1550k_output.csv
- shaft_min_h_low_str_CSR_0.0004_broken_joint_1550k_WKS.mat
- Template_StateFile.pvsm
- WKS.mat

Tab. A-1: Summary of HLW emplacement tunnel simulations performed in this study

No.	Folder name
	HLW drifts
01	1. HLW_min_h_low_str_CSR_0.0025_aniso_output
02	2. HLW_min_h_upp_str_CSR_0.001_aniso_output
03	3. HLW_ref_h_low_str_CSR_0.002_aniso_output
04	4. HLW_ref_h_upp_str_CSR_0.0015_aniso_output
05	5. HLW_max_h_low_str_CSR_0.004_aniso_output
06	6. HLW_max_h_upp_str_CSR_0.003_aniso_output
07	7. HLW_max_h_low_str_CSR_El_0.0005_Et_0.05_output
09	8. HLW_min_h_low_str_CSR_El_0.0005_Et_0.04_output
09	9. HLW_ref_h_low_str_CSR_El_0.0005_Et_0.04_output
	L/ILW caverns
10	1. ILW_min_h_low_str_CSR_0.0025_aniso_output
11	2. ILW_min_h_upp_str_CSR_0.001_aniso_output
12	3. ILW_ref_h_low_str_CSR_0.003_aniso_output
13	4. ILW_ref_h_upp_str_CSR_0.00165_aniso_output
14	5. ILW_max_h_low_str_CSR_0.004_aniso_output
15	6. ILW_max_h_upp_str_CSR_0.00375_aniso_output
16	7. ILW_max_h_low_str_CSR_El_0.0008_Et_0.06_output
17	8. ILW_min_h_low_str_CSR_El_0.0005_Et_0.04_output
18	9. ILW_ref_h_low_str_CSR_El_0.0005_Et_0.04_output
	Shafts
19	1. shaft_min_h_low_str_CSR_0.0004_aniso_output
20	2. shaft_min_h_upp_str_CSR_0.0001_aniso_output
21	3. shaft_ref_h_low_str_CSR_0.00045_aniso_output
22	4. shaft_ref_h_upp_str_CSR_0.0001_aniso_output
23	5. shaft_max_h_low_str_CSR_0.00095_aniso_output
24	6. shaft_max_h_upp_str_CSR_0.0005_aniso_output
25	7. shaft_max_h_low_str_CSR_0.007_output
26	8. shaft_min_h_low_str_CSR_0.004_output
27	9. shaft_ref_h_low_str_CSR_0.004_output

Tab. A-2: Png graphics identifier

File type / extension	File name	Content
Input files	Namefolder_broken_joint_1550k_output.csv	Geomechanica input file, with columns: • Fracture ID • (x0,y0) to (x3,y3): coordinates of the four points defining the polygon • Failure mode: 1, 2 or 3 • Area: fracture area (will be recalculated) • Length: fracture length (will be recalculated)
	Namefolder_broken_joint_1550k_WKS.mat	Matlab workspace containing Geomechanical inputs for fast reading
Parameter files	Meshparams.dat	Text file containing the definition of the radial mesh. Parameters are described in the file
	params.dat	Text file containing the parameters for upscaling. Parameters are described in the file
Auxiliary files	AllFractures_Stats.out Mode1Fractures_Stats.out Mode2Fractures_Stats.out	Text files containing basic statistics of all fractures, and of fractures grouped by failure mode. Variables observed are: • Total number of fractures or of fractures of one kind • Length, inclination, aperture and transmissivity
	Abstraction_EDZ_ini.txt Abstraction_EDZ_end.txt	Final upscaling outputs: EDZ equivalent radius, hydraulic conductivity and porosity
Output files	Equiv_K_Phi_q.xlsx	Excel files containing 1D profiles of integrated outputs. Columns: A = radial distance from centre B = Total axial flux (initial) C = Total axial flux after resaturation D = Total porosity E = Fracture density F = Axial flux across fractures (initial) G = Axial flux across fractures after resaturation H = Porosity of fractures (initial) I = Porosity of fractures after resaturation J = Porosity of matrix (initial) K = Porosity of matrix after resaturation
	WKS.mat	Matlab workspace file containing all outputs

Tab. A-2: Cont.

File type / extension	**File name**	**Content**
png graphics	Cell_Code.png	Colour code: green = liner red = EDZ element with fractures blue = intact OPA
	DFN.png	EDZ geometry, as read by the code
	Fracdens.png	2D coloured map of fracture density
	Fracture density.png	Integrated fracture density vs radial distance
	Integrated porosity.png	Integrated porosity vs radial distance at early and late times (fracture, matrix and total porosities)
	DFN.png	EDZ geometry, as read by the code
	Fracdens.png	2D coloured map of fracture density
	Fracture density.png	Integrated fracture density vs radial distance
	Integrated porosity.png	Integrated porosity vs radial distance at early and late times (fracture, matrix and total porosities)
	Ktot_ini.png	2D coloured map of initial hydraulic conductivity
	K_tot_end.png	2D coloured map of final hydraulic conductivity (after resaturation)
	K_f_ini.png	2D coloured map of fracture initial hydraulic conductivity
	K_f_end.png	2D coloured map of fracture final hy-draulic conductivity (after resaturation)
	K_m_ini.png	2D coloured map of matrix initial hydraulic conductivity
	K_m_end.png	2D coloured map of matrix final hy-draulic conductivity (after resaturation)
	Nfracs.png	2D coloured map of number of fractures at each element
	P21.png	2D coloured map of fracture intensity
	Poro.png	2D coloured map of total porosity (constant in time)
	Poro_f_ini.png	2D coloured map of initial fracture porosity
	Poro_f_end.png	2D coloured map of final fracture porosity
	Poro_m_ini.png	2D coloured map of initial matrix porosity
	Poro_m_end.png	2D coloured map of final matrix porosity

Tab. A-2: Cont.

File type / extension	File name	Content
	Radial_Mesh.png	Radial mesh utilized in the calculations. The liner is depicted in green and elements inside are removed afterwards.
	Radius_EDZ.png	Abstracted radius of the EDZ and equivalent parameters
	Namefolder.png	EDZ geometry, as supplied by Geomechanica. Note the variable name of file (same as folder). It is identical to DFN.png.
	Specific axial fluxes.png	Specific axial fluxes vs radius at early and late times (green and red curves, resp.) across fractures only (left panel) and total (i.e., including the fluxes in the matrix, right panel)
	Stats_DFN.png	Histograms of geometric features of the EDZ considering all fractures together
	Stats_DFN_BreakMode_1.png	Histograms of geometric features of the EDZ. Mode 1 of opening only.
Paraview files	Namefolder_broken_joint_1550000.vtu	Paraview files as supplied by Geomechanica
	FEMDEM.vtk	Geometry of the fractures forming the EDZ, defined as four-point polygons, and associated properties (failure mode, length, inclination, area, initial aperture, irreducible (final) aperture, log10 of initial and final transmissivities, and fracture id in the Geomechanica input file
	GridProps.vtk	Upscaled EDZ properties: • Initial and final hydraulic conductivities of fracture and matrix, resp. kf_ini, kf_end, km_ini and km_end • Initial and final total hydraulic (Conductance_ini and Conductance_end) • Initial and final porosities of fracture and matrix, resp. phif_ini, phif_end, phim_ini and phim_end • Total porosity (Porosity; does not vary in time) • Number of fractures per element (NCounts) • Fracture intensity (P21) • Fracture density (Fracdens) • Cell code (liner =1, fractured = 2, intact OPA = 3)

Tab. A-2: Cont.

File type / extension	File name	Content
	Liner.vtk	Just a line depicting the outer trace of the liner
	Template_StateFile.pvsm	Paraview State file loading all vtk files together
Origin data base	EDZ-Site-Specific-HLW-LILW.obju	Graphical output files for NAB 25-03

Text in italics is different in each folder. The file name is similar to the folder name.